

p, He, and C to Fe cosmic-ray primary fluxes in diffusion models

Source and transport signatures on fluxes and ratios.

A. Putze¹, D. Maurin^{2,3,4,5}, and F. Donato⁶

¹ The Oskar Klein Centre for Cosmoparticle Physics, Department of Physics, Stockholm University, AlbaNova, SE-10691 Stockholm, Sweden

² Laboratoire de Physique Subatomique et de Cosmologie (LPSC), Université Joseph Fourier Grenoble 1, CNRS/IN2P3, Institut Polytechnique de Grenoble, 53 avenue des Martyrs, Grenoble, 38026, France

³ Laboratoire de Physique Nucléaire et des Hautes Energies, Universités Paris VI et Paris VII, CNRS/IN2P3, Tour 33, Jussieu, Paris, 75005, France

⁴ Dept. of Physics and Astronomy, University of Leicester, Leicester, LE17RH, UK

⁵ Institut d'Astrophysique de Paris, UMR7095 CNRS, Université Pierre et Marie Curie, 98 bis bd Arago, 75014 Paris, France

⁶ Dept. of Theoretical Physics and INFN, via Giuria 1, 10125 Torino, Italy

Received / Accepted

ABSTRACT

Context. The source spectrum of cosmic rays is not well determined by diffusive shock acceleration models. The propagated fluxes of proton, helium, and heavier primary cosmic-ray species (up to Fe) are a means to indirectly access it. But how robust are the constraints, and how degenerate are the source and transport parameters?

Aims. We check the compatibility of the primary fluxes with the transport parameters derived from the B/C analysis, but also if they bring further constraints. We study whether the shape of these fluxes and their ratios are mostly driven by source or propagation effects. We then derive the source parameters (slope, abundance, and low-energy shape).

Methods. Simple analytical formulae are used to address the issue of degeneracies between source/transport parameters, and to understand the shape of the p/He and C/O to Fe/O data. The full analysis relies on the USINE propagation package, the MINUIT minimisation routines (χ^2 analysis) and a Markov Chain Monte Carlo (MCMC) technique.

Results. Proton data are well described in the simplest model defined by a power-law source spectrum and plain diffusion. They can also be accommodated by models with, e.g., convection and/or reacceleration. There is no need for breaks in the source spectral indices below ~ 1 TeV/n. Fits on the primary fluxes alone do not provide physical constraints on the transport parameters. If we let free the source spectrum $dQ/dE = q\beta^{\eta_S}\mathcal{R}^{-\alpha}$ and fix the diffusion coefficient $K(R) = K_0\beta^{\eta_T}\mathcal{R}^\delta$ such as to reproduce the B/C ratio, the MCMC analysis constrains the source spectral index α to be in the range 2.2 – 2.5 for all primary species up to Fe, regardless of the value of the diffusion slope δ . The η_S low-energy shape of the source spectrum is degenerate with the low-energy shape η_T of the diffusion coefficient: we find $\eta_S - \eta_T \approx 0$ for p and He data, but $\eta_S - \eta_T \approx 1$ for C to Fe primary species. This is consistent with the toy-model calculation in which the shape of the p/He and C/O to Fe/O data is reproduced if $\eta_S - \eta_T \approx 0 - 1$ (no need for different slopes α). When plotted as a function of the kinetic energy per nucleon, the low-energy p/He ratio is shaped mostly by the modulation effect, whereas primary/O ratios are mostly shaped by their destruction rate.

Conclusions. Models matched on B/C are compatible with primary fluxes. The different spectral indices for the propagated primary fluxes up to a few TeV/n can be naturally ascribed to transport effects only (universality of source spectra).

Key words. Methods: statistical – ISM: cosmic rays

1. Introduction

The measured galactic cosmic-ray (GCR) fluxes at Earth result from a three-step journey: i) the diffusive shock acceleration (DSA) mechanism provides a source spectrum; ii) these fluxes are then transported (diffusion, but also convection and reacceleration) and also interact in the ISM until they reach the Solar neighbourhood; iii) they enter the solar cavity where they decelerate due the effect of the solar modulation (active for GCRs below a few tens of GeV/n).

The last step prevents us a direct access to low-energy (beyond a few hundreds of GeV/n) interstellar fluxes (IS).

The first step is inspected by means of semi-analytical or numerical studies of the DSA mechanism. However, due to the variety of possible sources for the GCRs, and the intrinsic difficulties of this mechanism, the source spectral index and especially its low-energy shape is not very well predicted (e.g., Caprioli et al. 2010). Awaiting further progress along this line, an indirect route to access the source spectrum is to start with the top-of-atmosphere (TOA) fluxes and go back to the source spectra. To do so, it is generally assumed that the steady state holds for the propagation, and that the first and second step are independent. The first assumption is known to fail at high enough energy, whereas the second one may only be approximate. In

Send offprint requests to: A. Putze, antje@fysik.su.se

this study, given the success of simple steady-state diffusion models for the nuclear component, we follow the same route in order to draw some constraints on the source parameters.

The propagation step is the focus point of many phenomenological studies interested in the flux of secondary species (created by means of the interaction of the primary species in the ISM and radiation field of the Galaxy) such as some light nuclei, antiprotons, positrons, radioactive isotopes and also gamma rays. The transport parameters are usually determined by fitting data on primary-to-secondary nuclei, as for example the B/C (boron-to-carbon) ratio. However, present data on B/C ratio, even when combined with radioactive isotope measurements, leave a constrained, yet large range of allowed values for these parameters (Maurin et al. 2001, 2010; Putze et al. 2010). The study of these secondary-to-primary ratios is—to first order—insensitive to the details of the source spectra (e.g., Maurin et al. 2002). Therefore, a common phenomenological approach is to first extract the transport parameters, then to fit the source spectra, although the source and transport parameters may be correlated (Putze et al. 2009).

The importance of the primary fluxes and their ratio was recognised some time ago (Webber & Lezniak 1974). In this paper we reconsider their use, trying to answer the following questions: what phenomena shape the TOA and IS fluxes? Is it the source spectrum or the propagation step, and are there degeneracies between the two effects? To which accuracy can we determine the low-energy source spectra, the spectral indices, and the source abundances? Are the source spectra universal or species dependent?

On the experimental side, we dispose of accurate data up to few hundreds of GeV, whilst at higher energies data are less abundant and with large error bars and scatter. On the modelling side, we have a semi-analytical propagation model proved to work well with many GCR observables (Maurin et al. 2001; Donato et al. 2001, 2002, 2009) and an implementation of the Markov Chain Monte Carlo technique (MCMC) to get the probability density functions of the analysed parameters (Putze et al. 2009, 2010). We take advantage of these to address the above questions. Our results are also supported by toy-model calculations, especially for the shape of ratio p/He. As abundant and accurate data are expected in the near future by the orbiting PAMELA experiment and forthcoming AMS-02 detector (to be installed on the International Space Station), such a study also aims at providing some guidelines on how to tackle the information contained in the primary flux propagated spectra.

The paper is organised as follows: Sect. 2 contains a short overview of the propagation scheme employed in the present study. In Sect. 3, we discuss the p and He data and whether they can provide any constraints on the transport parameters or if they can be fitted in any propagation configuration (i.e. w/wo convection, w/wo reacceleration). In Sect. 4, we seek for generic constraints on the source spectra (p, He, and C to Fe) comparing the values obtained in different configurations of propagation models. In Sect. 5, the origin for the observed shape for the ratio of primary species is outlined. Our conclusions and perspectives are given in Sect. 6.

2. The propagation model

The framework employed to calculate the fluxes is the diffusion model with convection and reacceleration discussed in Maurin et al. (2001, 2002), updated and fully detailed in Putze et al. (2010). Here we only remind the main features.

The Galaxy is shaped as a baryonic thin disk with half-thickness $h = 0.1$ kpc and an infinite radial extension (1D model, as also used in Jones et al. 2001), hosting the interstellar medium and the stars, and surrounded by a diffusive thick halo whose half-height is L .

Assuming steady-state, the transport equation for the nucleus j can be written as

$$\mathcal{L}^j N^j + \frac{\partial}{\partial E} \left(b^j N^j - c^j \frac{\partial N^j}{\partial E} \right) = \mathcal{S}^j .$$

where the differential density $N^j \equiv N^j(E, \mathbf{r})$ depends on the position \mathbf{r} in the Galaxy and on the energy (throughout the paper, E is the total energy, E_k is the kinetic energy, $E_{k/n}$ the kinetic energy per nucleon, and $E_{/n}$ the total energy per nucleon). \mathcal{L}^j sums up the physics of the transport in the Galaxy, while \mathcal{S}^j contains the source term.

2.1. Transport parameters

The operator \mathcal{L} (we omit the superscript j) describes the diffusion $K(\mathbf{r}, E)$ and convection $\mathbf{V}(\mathbf{r})$ in the Galaxy, the decay rate $\Gamma_{\text{rad}}(E) = 1/(\gamma\tau_0)$ for radioactive species, and the destruction rate $\Gamma_{\text{inel}}(\mathbf{r}, E) = \sum_{ISM} n_{\text{ISM}}(\mathbf{r}) v \sigma_{\text{inel}}(E)$ on the interstellar matter (ISM). It reads

$$\mathcal{L}(\mathbf{r}, E) = -\nabla \cdot (K \nabla) + \nabla \cdot \mathbf{V}_C + \Gamma_{\text{rad}} + \Gamma_{\text{inel}} .$$

The spatial diffusion coefficient is parametrised as

$$K(E) = \beta^{\eta_T} \cdot K_0 \mathcal{R}^\delta . \quad (1)$$

where $\mathcal{R} = pc/Ze$ is the rigidity of the particle, β is the velocity of the particle in units of c and the default value for η_T is 1. Ptuskin et al. (2006) argued that the form of the spatial diffusion coefficient could be modified at low energy, due to the possibility that the nonlinear MHD cascade sets the power-law spectrum of turbulence. Indeed, Maurin et al. (2010) found that the value of this parameter was crucial for the determination of δ given the current B/C data. The convective wind acts in the whole diffusive volume with a constant velocity $\mathbf{V}_C = \pm V_C \mathbf{e}_Z$ pointing perpendicularly to the galactic disk. The coefficients b and c account for the first and second order energy changes

$$\begin{aligned} b(\mathbf{r}, E) &= \left\langle \frac{dE}{dt} \right\rangle_{\text{ion, coul.}} - \frac{\nabla \cdot \mathbf{V}}{3} E_k \left(\frac{2m + E_k}{m + E_k} \right) \\ &\quad + \frac{(1 + \beta^2)}{E} \times K_{pp}, \\ c(\mathbf{r}, E) &= \beta^2 \times K_{pp}. \end{aligned}$$

Coulomb and ionisation losses add to possible energy gains due to reacceleration, described by the coefficient K_{pp} in momentum space. The parameterisation for K_{pp} is taken from the model of minimal reacceleration by the interstellar turbulence (Osborne & Ptuskin 1988; Seo & Ptuskin 1994):

$$K_{pp} \times K = \frac{4}{3} V_a^2 \frac{p^2}{\delta (4 - \delta^2) (4 - \delta)} . \quad (2)$$

where V_a is the Alfvénic speed.

2.2. Source parameters

The source term \mathcal{S} includes the initial spectrum at source and the secondary contributions (spallations of heavier nuclei). Acceleration models typically predict $dQ/dp \propto p^{-\alpha}$ (e.g., Jones 1994), which leads to $dQ/dE \propto p^{-\alpha}/\beta$, where the low-energy behaviour is unknown. For further usage, we remind that

$$\frac{dQ}{dE} = \frac{dQ}{dE_k} = \frac{1}{A} \cdot \frac{dQ}{dE_{k/n}} = \frac{1}{\beta} \cdot \frac{dQ}{dp} = \frac{1}{Z\beta} \cdot \frac{dQ}{dR}. \quad (3)$$

In this paper, we model the low-energy shape by adding one free parameter, η_S , active at low energy:

$$Q_{E_{k/n}}(E) \equiv \frac{dQ}{dE_{k/n}} = q \cdot \beta^{\eta_S} \cdot \mathcal{R}^{-\alpha}, \quad (4)$$

where q is taken to be the normalisation for a differential energy per nucleon source spectrum. The reference low-energy shape corresponds to $\eta_S = -1$ (to have $dQ/dp \propto p^{-\alpha}$, i.e. a pure power-law).

2.3. Free parameters of the model

The present model contains a priori several free parameters. The parameters in the transport sector $\{K_0, \delta, V_a, V_c, \eta_T\}$, the ones in the source term $\{q, \eta_S, \alpha\}$ and the halo size of the Galaxy L . We will see in the following of the paper that not all these parameters have the same relevance in the physics of primary cosmic nuclei, and we will therefore operate within a critical sub-sample. In diffusion models, L cannot be solely determined from the B/C ratio because of the well-known degeneracy between K_0 and L when only stable species are considered. If not differently stated, we will work with the default values $\eta_S = -1$ and $\eta_T = 1$, and the reference value $L = 4$ kpc. In most of the analyses we let free the source normalisation q_i for each primary species.

The low energy ($\lesssim 10$ GeV/n) charged particles are braked in the heliosphere by the solar wind, modulated according to an 11-year cycle. We adopt the force-field approximation, which provides a simple analytical one-to-one correspondence between the modulated top-of-the-atmosphere (TOA) and the demodulated interstellar (IS) fluxes. For a species j , the IS and TOA energies per nucleon are related by $E_{/n}^{\text{IS}} = E_{/n}^{\text{TOA}} + \Phi$ ($\Phi = Z/A \times \phi$ is the modulation parameter), and the fluxes by (p is the momentum)

$$\psi^{\text{IS}}(E^{\text{IS}}) = \left(\frac{p^{\text{IS}}}{p^{\text{TOA}}} \right)^2 \psi^{\text{TOA}}(E^{\text{TOA}}). \quad (5)$$

This effect is taken into account according to the well known force-field approximation, whose only effective parameter is the modulation potential ϕ (GV).

3. Analysis with free source and transport parameters

In this Section, we use different data sets on proton and helium fluxes¹ in order to outline which propagation models

¹ The isotopic separation is not always achieved, so that many data actually correspond to ${}^1\text{H}+{}^2\text{H}$ for the proton flux and ${}^3\text{He}+{}^4\text{He}$ for the helium flux, where ${}^2\text{H}$ and ${}^3\text{He}$ come from secondary contributions only. This amounts to a $\lesssim 10\%$ error at low energy, which is contained in the error bars.

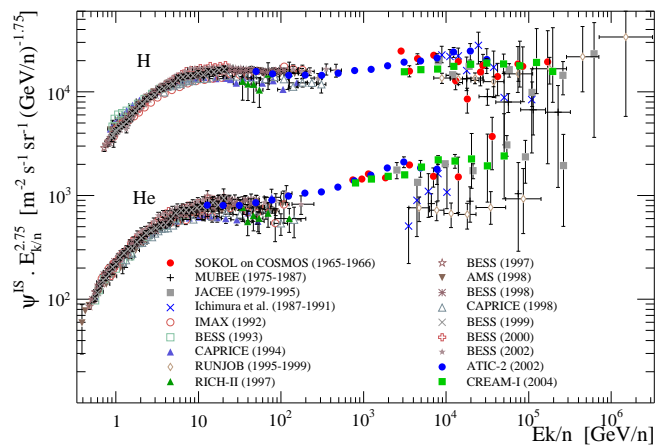


Fig. 1. Demodulated p and He data ($\times E_{k/n}^{2.75}$) as a function of $E_{k/n}$. The low-energy data and the associated modulation parameter are: AMS-01 (Alcaraz et al. 2000 for H and AMS Collaboration et al. 2000 for He) with $\phi = 600$ MV; CAPRICE94 (Boezio et al. 1999) and CAPRICE98 (Boezio et al. 2003) with $\phi = 650$ MV and 600 MV respectively; IMAX (Menn et al. 2000) with $\phi = 750$ MV; and the series of BESS balloon flights BESS93 (Wang et al. 2002) BESS97 (Shikaze et al. 2007), BESS98 (Sanuki et al. 2000; Shikaze et al. 2007), BESS99 (Shikaze et al. 2007), BESS00 (Shikaze et al. 2007), and BESS02 (BESS-TeV, Haino et al. 2004; Shikaze et al. 2007), for which $\phi = 700$ MV, 491 MV, 591 MV, 658 MV, 1300 MV, 1109 MV respectively. The intermediate and high-energy data are: ATIC-2 (Panov et al. 2009), CREAM-I (Ahn et al. 2010a), JACEE (Asakimori et al. 1998), MUBEE (Zatsepin et al. 1993), RICH-II (Diehl et al. 2003), RUNJOB (Derbina et al. 2005), SOKOL (Ivanenko et al. 1993), and Ichimura et al. (1993).

explain data and try to set constraints on the free parameters of our model. The fitting procedure is based on the MINUIT routine, which traces back a χ^2 .

3.1. Data

A first important matter is the choice of the data to fit the models. The top panel in Fig. 1 shows the available data on p and He fluxes. The abscissa is the kinetic energy per nucleon ($E_{k/n}$) and the ordinate $\psi^{\text{IS}} \times E_{k/n}^{2.75}$, where ψ^{IS} is the IS, demodulated using the force-field approximation. The low-energy region (below 100 GeV/n) has been covered by many balloon-borne, shuttle-based and satellite experiments, whereas above a few TeV/n the data come from several balloon long-exposure flights (accumulated over several flights in a decade). ATIC data cover the gap at a few TeV/n energy. The overall agreement between the data is fair, the scatter between the data being higher at high energy.

For our analysis, the criterion is to select data samples covering a broad energy range and consistent with each others. We show a subset of demodulated data in Fig. 2 to emphasise on the error bars and differences between the most recent and consistent sets of p and He data, namely AMS-01 (Alcaraz et al. 2000; AMS Collaboration et al.

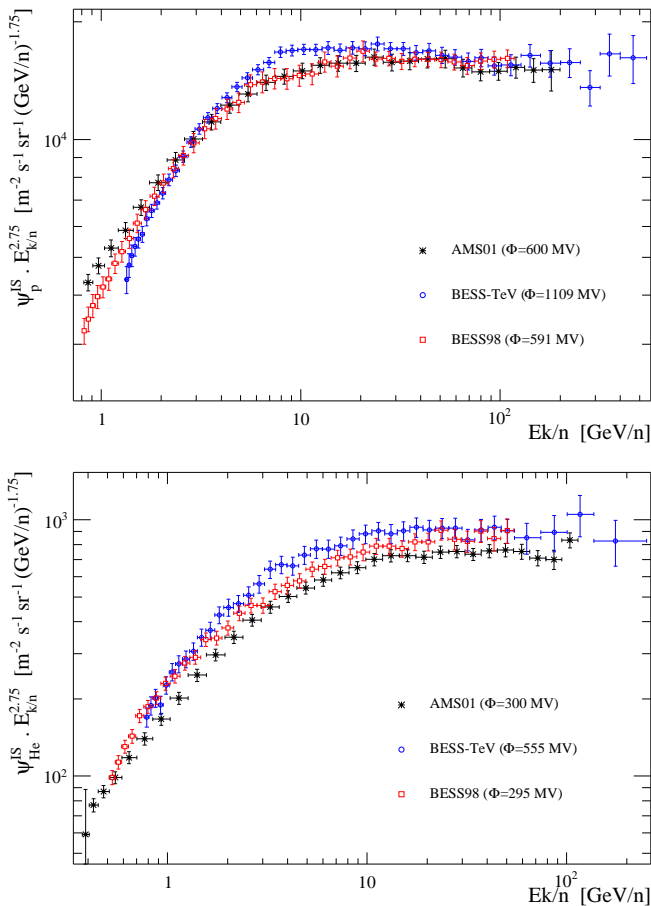


Fig. 2. Demodulated p (top panel) and He (bottom panel) flux $\times E_{k/n}^{2.75}$ as a function of $E_{k/n}$ for AMS-01 (black stars), BESS98 (empty red squares) and BESS-TeV (empty blue circles).

2000), BESS98 (Sanuki et al. 2000; Shikaze et al. 2007) and BESS-TeV (a.k.a. BESS02, Haino et al. 2004; Shikaze et al. 2007). For the proton flux, the AMS-01 and BESS98 data, both taken in 1998 in the same solar period, are consistent except at low energy. BESS-TeV data taken in 2002 during a high solar level show a different behaviour at low and intermediate energy. Note that usually the solar modulation level is obtained by fitting ϕ and a simple two-parameter proton spectrum to the data (Shikaze et al. 2007). This is the standard lore in the field, although it is expected to give biased modulation level (for example, we do not know the true proton spectrum, there is the problem of polarity in the solar magnetic field, etc). The goal of the paper is not to deal with these issues, but the fact that the proton data are already inconsistent among themselves implies that we may expect inconsistencies in the fitted models.

3.2. Pure diffusive transport

The first step is to test a minimal model containing only acceleration and plain diffusion, as well as nuclear reactions and electromagnetic energy losses, but without convection and reacceleration ($V_a = V_c = 0$).

Table 1. Best-fit to p and He data for pure diffusive transport (experiment, number of data, best χ^2 /d.o.f., and best-fit $\alpha + \delta$ value).

Data	p			He		
	#	$\frac{\chi^2}{\text{d.o.f.}}$	$\alpha + \delta$	#	$\frac{\chi^2}{\text{d.o.f.}}$	$\alpha + \delta$
AMS-01 (1)	28	0.19	2.99	31	0.72	2.81
BESS98 (2)	41	0.39	2.99	36	0.36	2.77
BESS-TeV (3)	47	0.72	2.89	40	0.80	2.80
(1 + 2)	69	0.66	3.00	67	1.75	2.81
(1 + 2 + 3)	116	1.95	2.99	107	2.52	2.81
All LE [†]	304	6.22	2.96	287	2.77	2.79
ATIC-2	15	22.46	2.75	15	37.4	2.81
All HE*	59	2.58	2.87	39	4.18	2.85

[†] IMAX92, BESS93, CAPRICE94, BESS97, AMS-01, BESS98, CAPRICE98, BESS99, BESS00, BESS02.

* CREAM, SOKOL, MUBEE, JACEE, Ichimura et al., RUNJOB.

Main degeneracies In pure diffusion model, the flux of any primary species at high energy can be approximated by²

$$\psi(E) \propto \frac{Q(E)}{K(E)} \propto \frac{q}{K_0} \cdot E^{-(\alpha+\delta)}. \quad (6)$$

This formula shows two degeneracies between the source and transport parameters: the first one is in the normalisation q/K_0 , the second one is in the spectral total index $\alpha + \delta$.

We start with a minimisation procedure setting the free parameters δ, α and $q_{p,He}$ (in order to break the degeneracy between q and K_0 the latter is set to $0.0048 \text{ kpc}^2 \text{ Myr}^{-1}$). The results are presented for the proton and He in two different columns in Table 1. The $\chi_{\text{min/d.o.f.}}^2$ values are very small for a number of cases, indicating a possible overfitting of the data. The value of the best-fit parameters are not reported since they are not relevant at this stage of the analysis. For the different sets of data, the values of both α and δ vary from almost any value between 0 and 2.8 (not shown in the Table), but the sum of them is close to 3.0 for p and 2.8 for He. The first three lines show that a fit to p and He on the AMS or BESS data is always possible in a simple diffusion scheme (although it provides unphysical values for α and δ). The fourth line shows the combined analysis of AMS-01 (Alcaraz et al. 2000) and BESS98 (Sanuki et al. 2000) data. They have been collected in the same year (1998)—which may help reduce the systematics due to solar wind modelling—and span nearly the same energy range. The $\chi_{\text{min/d.o.f.}}^2 = 1.75$ for the fit of combined He data, compared to the respective $\chi_{\text{min/d.o.f.}}^2$ values of 0.72 and 0.36 for separate data shows inconsistencies among the data sets, as underlined in Sect. 3.1. When combining the three experiments (fifth line), this is even more visible, also for protons (the best-fit slope is unaffected). We have fitted also all the available data in the low energy (sixth line) and in the highest energy range (last line). The agreement among the data sets is poor, both for protons and helium, as already visible in Fig. 1. ATIC data, which connect the

² Throughout the paper, the quantity ψ denotes the differential flux in kinetic energy per nucleon, i.e. $d\psi/dE_{k/n}$. The notation $d\psi/d\mathcal{R}$ used in Sect. 5 is the only place where it will refer to the differential flux in rigidity.

low and high energy sectors, are badly fit by any pure diffusive model.

We may naively interpret the results of Table 1 as the fact that p and He data can be well accommodated in any purely diffusive transport models, in the low energy range ($\lesssim 100$ GeV/n), for each experimental data set taken separately. But such models lead to unphysical values for δ and α . So it could also mean that the hypothesis of a standard source spectrum (i.e., $dQ/dp \propto \mathcal{R}^{-\alpha}$ when setting $\eta_S = -1$) and a standard propagation scheme ($\eta_T = 1$) is unsupported by the data, or that additional effects (e.g., convection and/or reacceleration) are required to match the data. Before resolving this issue, we go further with the comparison of the approximated formulae and the full calculation.

Inelastic interaction: a link between α , δ and K_0 . Getting explicit the effect of the catastrophic losses at low energy, Eq. (6) gives, for a 1D model,

$$\psi(E) = \frac{v}{4\pi} \cdot \frac{Q(E)}{\frac{K_0 \beta \mathcal{R}^\delta}{hL} + n_{\text{ISM}} \sigma v}. \quad (7)$$

For δ fixed, Eq. (7) implies a correlation between K_0 , α and δ , given some primary data. Indeed, as K_0 decreases, the inelastic interaction term $n_{\text{ISM}} \sigma v$ becomes more efficient in the denominator of Eq. (7). The effect of the species destruction is therefore more pronounced at low energy. Fixing δ and going to small K_0 we expect that, in order to balance the increased destruction rate, the numerator tunes and α is decreased. If K_0 is fixed and small, so that inelastic interactions can be dominant, the same amount of protons (or helium) can be obtained with a larger $\alpha + \delta$.

This effect is confirmed by the numerical results, as visible in Fig. 3. For each point in the $K_0 - \delta$ plane, we plot $\alpha + \delta$ for the best-fit model on AMS-01 proton data (the free parameters are α and q_p). We checked (not shown) that similar values for $\alpha + \delta$ are obtained when the fits is performed on other proton fluxes (BESS98 or BESS-TeV), or for other species (He or a combined fit p+He). We can see from the figure that, for any fixed δ value, the data require higher $\alpha + \delta$ while K_0 decreases, namely while the reaction rate gets more and more relevant. This effect is less pronounced for small values of the diffusion coefficient slope, namely when δ is close to 0.2-0.3.

Asymptotic behaviour (or why $\alpha + \delta \gtrsim \gamma_{\text{data}}$) Even for light primary species such as protons, which suffer the less from destruction in the ISM, the asymptotic purely diffusive regime is not reached. If we fit a primary flux with (as is usually done in the literature)

$$\psi(E) \propto E^{-\gamma_{\text{data}}},$$

then we are bound to have

$$\alpha + \delta \equiv \gamma_{\text{asympt}} \gtrsim \gamma_{\text{data}}.$$

This implies that caution is in order whenever we wish to compare the result of studies fitting the propagated fluxes with a power-law function (e.g., Shikaze et al. 2007) to those (such as this one) fitting directly the source spectrum. Catastrophic, but also continuous losses flatten the propagated spectrum below \lesssim few tens of GeV/n energies.

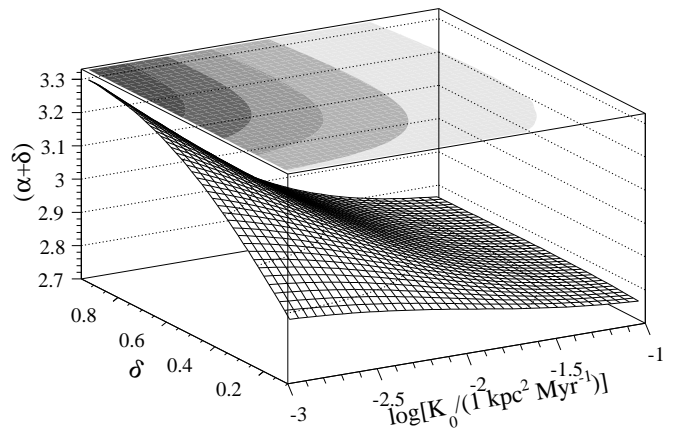


Fig. 3. Surfaces of $\alpha + \gamma$ for the best-fit models in the plane $K_0 - \delta$ (free parameters are α and q_p) on AMS-01 proton data. The colour code (from light to darker shades) for the contours superimposed on top of each graph correspond to $(\alpha + \gamma) = \{2.8, 2.9, 3.0, 3.1, 3.2\}$.

The inequality $\gamma_{\text{asympt}} \gtrsim \gamma_{\text{data}}$ is also induced by convection and/or reacceleration, as obtained from a B/C analysis (Putze et al. 2010; Maurin et al. 2010).

Simultaneous fit of p and He to lift the $\alpha + \delta$ degeneracy? As the residence time—hence the destruction rate of any species—depends on the energy through the transport parameter δ (and not on $\alpha + \delta$), the different inelastic cross-section for each species ($\sigma_{\text{inel}}^p \sim 30$ mb and $\sigma_{\text{inel}}^{\text{He}} \sim 90$ mb) leave different imprints on the respective p and He low-energy spectrum. This is expected, to some degree, to lift the degeneracy on $\alpha + \delta$ when using a combined fit to various primary species.

Figure 4 shows the $\chi^2_{\text{min/d.o.f.}}$ contours in the $K_0 - \delta$ plane for the separate fits of p (first row), He (second row) and for the combined fit p+He (last row), for the different sets of data used before. The ranges chosen for K_0 and δ correspond to extreme but not impossible values of these parameters that can accommodate the secondary-to-primary B/C ratio (Maurin et al. 2010). The top-left plot shows the strong degeneracy of α and δ (for AMS-01 data), as almost any configuration is acceptable. The top-right plot shows that for other data (BESS-TeV) no good fit can be achieved ($\chi^2_{\text{min/d.o.f.}} > 2$) in the selected $K_0 - \delta$ region: the good fits occur for unrealistic δ only. We make notice here that there is no inconsistency with the results shown in Table 1, which have been obtained from spanning larger (and unphysical) ranges for the free parameters. The second row shows the fits on He data. All the experiments tend to prefer large K_0 and large δ (both unrealistic if we demand $\chi^2_{\text{min/d.o.f.}} \sim 1$), but the χ^2 keeps quite flat, meaning that no particular class of models is selected by helium data.

The third row of Fig 4 is the combined p+He fit. The resulting $\chi^2_{\text{min/d.o.f.}}$ surfaces corresponds to a trade-off between the best-fit for p and He. The best-fit δ (not shown in the figure) still falls in region of $\delta \gtrsim 1$, and the degeneracy $\alpha + \delta$ is not lifted as no specific value for δ is preferred.

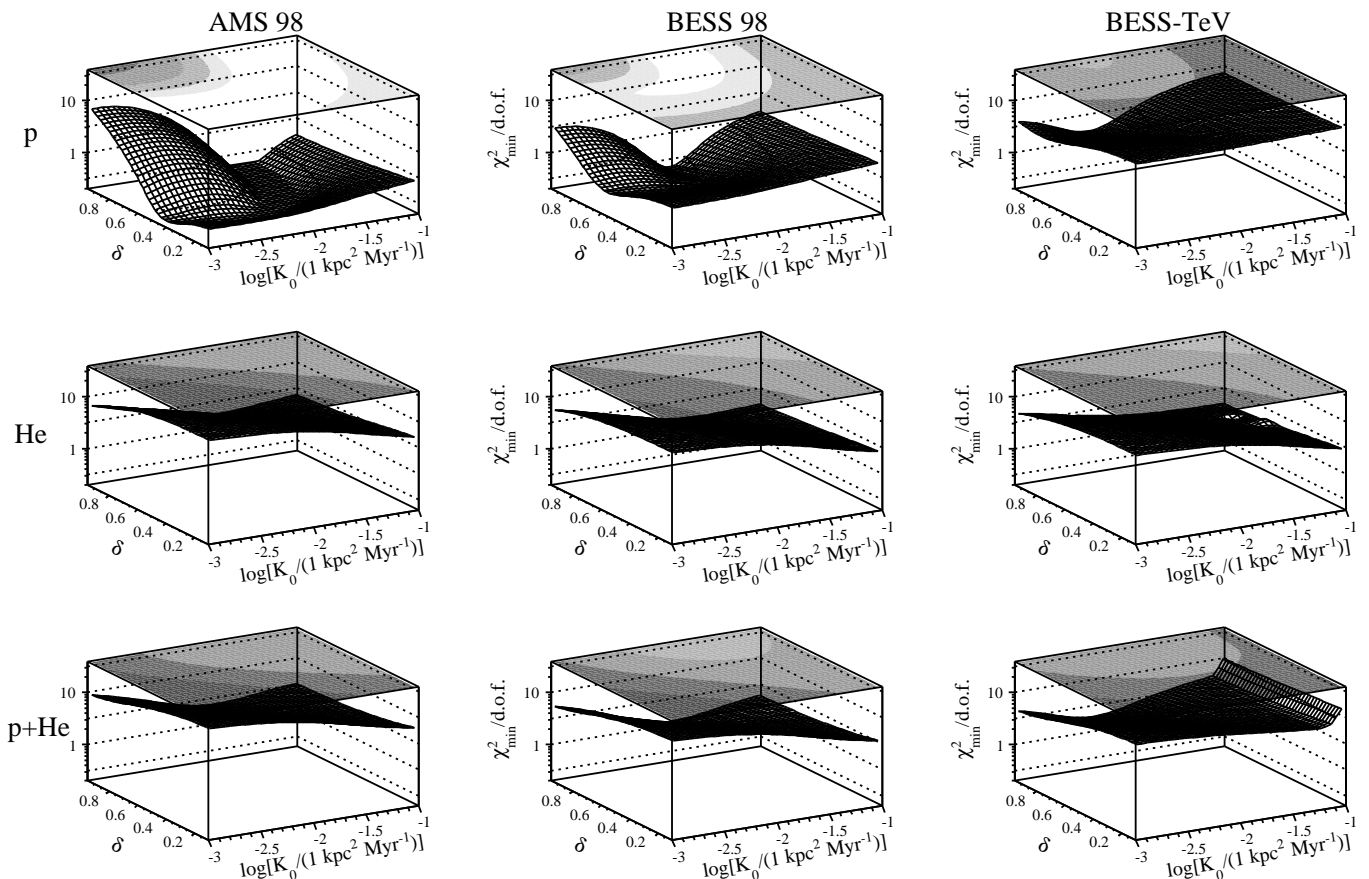


Fig. 4. Surfaces of $\chi^2_{\min}/\text{d.o.f.}$ (best-fit models) in the plane $K_0 - \delta$. First row: fit performed on p data (free parameters α and q_p). Second row fit performed on He data (free parameters α and q_{He}). Third row: fit performed simultaneously on p and He data (free parameters α , q_p and q_{He}). The columns from left to right correspond respectively to AMS-01, BESS88 and BESS-TeV data. The colour code for the contour plots (iso- $\chi^2_{\min}/\text{d.o.f.}$) superimposed on each graph is (from white to darker shades) $\chi^2_{\min}/\text{d.o.f.} = \{0.5, 1, 2, 5, 10\}$.

The role of η_S and η_T . We introduced the possibility to have a non-standard low-energy diffusion coefficient by means of the parameter η_T , see Eq. (1). The low-energy shape of the source spectrum is driven by the parameter η_S , see Eq. (4). If we neglect anew the nuclear interactions, we obtain—the extra β factor comes from the $v/4\pi$ in front of Eq. (7)—,

$$\psi(E) \propto \frac{Q(E)}{K(E)} \propto \beta^{\eta_S+1-\eta_T} \mathcal{R}^{-\alpha-\delta}. \quad (8)$$

The parameters η_S and η_T introduce a similar shape correction at the lowest energies. If it were not for energy losses and inelastic reactions (see next section), only the quantity $\eta_S - \eta_T$ would be expected to be constrained. We fit AMS-01 and BESS98 data, as well as all the proton data, with α , η_S , δ , and q_p as free parameters. The best χ^2 is slightly smaller than the one obtained with only α , δ , and q_p free (and $\eta_S = -1$). Similar results are achieved when the acceleration scheme is fixed to the standard lore ($\eta_S = -1$) and the fourth free parameter is η_T . However, as before, the corresponding values for the δ and α are again unsupported.

A further degeneracy can be brought by solar modulation, whose action is the decrease of the flux with the increase of the solar wind strength (parameter ϕ). On the other hand, the TOA flux increases with ϕ when $\eta_S \leq \eta_T$

(in the standard scenario $\eta_S = -1$ and $\eta_T = 1$), so that some compensation with solar modulation can be achieved.

3.3. Summary

The existing proton and helium data are unable to select any particular propagation model. This is consistent with the fact that the transport and source parameters are degenerate, as shown from simple arguments in our toy formulae. The best present data (AMS-01, BESS98 and BESS-TeV) can be quite well reproduced by solar modulated pure diffusive transport for instance, but they favour unphysical values of the source and transport parameters. Hence other ingredients are required. This could be a modification of the low-energy source spectrum or diffusion coefficient, or the addition of convection and/or reacceleration (that can accommodate as well the current data), or an improvement on the calculation of the solar modulation effect. However, given the present data and the physics of primary spectra, such an approach is bound to fail: the increase of the parameter space merely brings new degeneracies. Moreover, most of the parameter space is already ruled out by the B/C constraint. To go further, we thus have to restrict the parameter space to the source parameter space only (and use some prior on the propagation parameters).

4. Analysis with fixed transport parameters

We just showed that present data on primary fluxes alone cannot constrain significantly the transport parameters. The next natural strategy is to fit at the same time primary and secondary species. However, as emphasised in Putze et al. (2009), the large body of data for primary species drives the fit away from the best-fit regions of the B/C ratio. Actually, the standard lore to fix the transport parameters to their best-fit value, and then constrain the source parameters. But the latter values are then biased³. We nevertheless follow that approach, but we repeat the analysis on several possible transport configurations. This allows us to explicitly get the systematic variations (on the source parameters) related to this bias.

In this section, we first gather several sets of transport parameters shown to be consistent with B/C data (Sect. 4.1). We then fit the source parameters for p and He, the best-measured primary fluxes to date (Sect. 4.2). We repeat the analysis for other primary species, to inspect the universality of the source slopes and obtain their relative source abundances (Sect. 4.3).

4.1. Transport parameters consistent with B/C

The transport parameters are usually constrained from secondary-to-primary ratios (e.g. B/C). In the literature, various classes of models have been used, leading to very different values of their respective best-fit parameters. For instance, a model with diffusion + reacceleration is characterised by a best-fit propagation slope $\delta \approx 0.3 - 0.4$ (e.g., Lionetto et al. 2005), leaky-box inspired models points to $\delta \approx 0.5 - 0.6$ (e.g., Webber et al. 2003; Putze et al. 2009), whereas diffusion + convection models (w/wo reacceleration) points to $\delta \approx 0.75 - 0.85$ (e.g., Maurin et al. 2001; Putze et al. 2010).

This sensitivity to the CR transport mode (pure diffusion, w/wo convection, w/wo reacceleration) is discussed in Maurin et al. (2010). Although the best-fit model is one with both convection and reacceleration, it predicts $\delta \sim 0.8$, a value quite high compared with theoretical expectations. Following Maurin et al. (2010), we use below four configurations of the diffusion model covering a large but plausible range for the transport parameters. These models along with their best-fit parameters are reproduced in Tab. 2:

- Model II is with reacceleration only;
- Model III is with convection and reacceleration;
- Model I/0 is with a low-energy upturn of the diffusion coefficient ($\eta_T < 0$);
- Model III/II is as I/0, but with reacceleration.

The first two models correspond to the best-fit parameters for a standard spatial diffusion coefficient [i.e. η_T set to 1, see Eq. (1)]. The last two lines correspond to a modified diffusion scheme: negative values of η_T are associated to an upturn of the diffusion coefficient at low energy (Ptuskin et al. 2006). These two models are respectively termed I/0 and III/II because both allow some convection, but both favour

³ Putze et al. (2009) show that the values of the source-spectrum parameters (slope and abundances) are positively correlated among themselves and with the reacceleration strength, but are negatively correlated with the other propagation parameters.

Table 2. Best-fit transport parameters for various configurations of the diffusion model (fitted on B/C data).

Model	η_T	$K_0^{\text{best}} \times 10^2$ (kpc ² Myr ⁻¹)	δ^{best}	V_c^{best} (km s ⁻¹)	V_a^{best} (km s ⁻¹)	$\chi^2/\text{d.o.f}$
II	1.	9.76	0.23	...	73.2	4.73
III	1.	0.48	0.86	18.8	38.0	1.47
I/0 [‡]	-2.6	2.05	0.61	0.	...	3.29
III/II	-1.3	3.16	0.51	0.	45.4	2.26

Note 1. These results were obtained for input ingredients described in Maurin et al. (2010), and for $L = 4$ kpc.

$V_c^{\text{best}} = 0$. As shown in Fig. 7 of Maurin et al. (2010), these models fit reasonably well the B/C data.

4.2. Constraints on p and He source parameters

4.2.1. Generalities

On the one hand, the low-energy shape of the source spectra are not well known theoretically. They result from the diffusive shock acceleration mechanisms at play in supernova (e.g. Drury 1983) or super-bubbles shocks (e.g. Ferrand et al. 2008). Power laws close to -2 (in energy space) are predicted at high energy, but there is still no agreement about the low-energy spectrum (e.g. Caprioli et al. 2010).

On the other end of the cosmic-ray journey, we have access only to propagated spectra, where effects such as destruction on the ISM, energy losses, galactic winds and reacceleration change the energy spectra up to a few tens of GeV/n. This is the route followed in this section, where we try to constrain the source parameters from a fit to the propagated fluxes. However, the shape of the flux at low-energy is only an extrapolation since the low-energy interstellar spectrum is screened by solar modulation effects.

Note that the low-energy (below 100 MeV) IS spectrum can be indirectly constrained, based on its interaction with the interstellar medium. In that case, the IS flux is based on empirical fits to the data (e.g., Herbst et al. 2010), and its extrapolation at low energy is used to calculate, e.g., the ionisation of the ISM (Webber 1987; Nath & Biermann 1994; Webber 1998) or and molecular clouds (Padovani et al. 2009), or the LiBeB galactic enrichment and production (Gilmore et al. 1992; Nath & Biermann 1994; Lemoine et al. 1998). Some of these studies conclude on an increase of the low-energy spectrum, but some others favour a flattening. Actually, data from the Voyager 1 & 2 spacecrafts near the heliospheric termination shock could also be helpful for such studies, as they are close to IS condition, their level of modulation being ≈ 60 MV (Webber et al. 2008; Webber & Highbie 2009). However, it has been argued recently that anomalous cosmic rays could contribute to an important fraction of the proton spectrum below 300 MeV (Scherer et al. 2008). For this reason, we do not include Voyager data in our fits, and will only compare them to the best-fit spectra (based on the other data) at the end of this section.

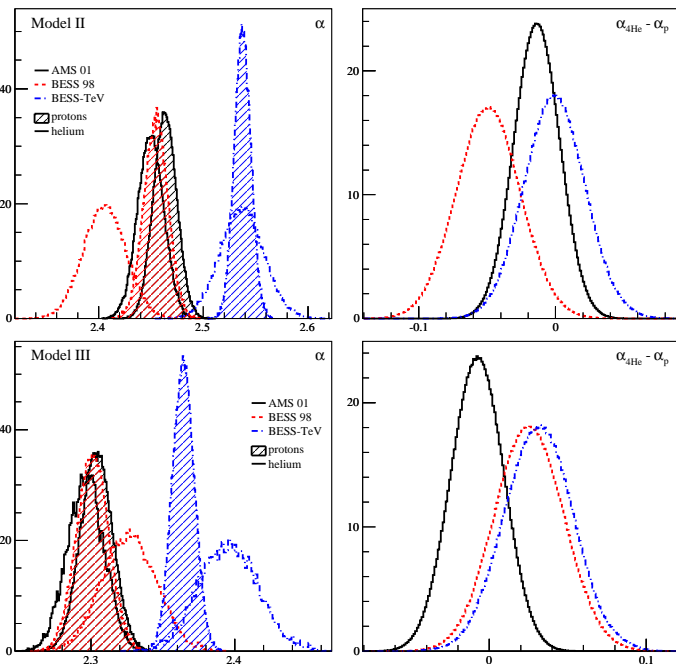


Fig. 5. Left panels: PDF of the source slope α for p (empty histograms) and He (hatched histograms). Right panels: PDF for $\alpha_{\text{He}} - \alpha_{\text{p}}$. The colour code corresponds to the three experimental data used: AMS-01 (solid black line), BESS98 (dashed red lines) and BESS-TeV (dash-dotted lines).

4.2.2. Results

Due to the lack of robust information about the low-energy spectrum, we choose to rely on a simple parametrisation allowing for an increase or decrease at low-energy, as given by Eq. (4), i.e. $Q_{E_{k/n}}(E) = q \cdot \beta^{\eta_S} \cdot \mathcal{R}^{-\alpha}$. For each configuration given in Table 2—i.e., for a given choice of the transport parameters K_0 , δ , η_T , V_a , and V_c —we then use the MCMC technique to get the probability density function (PDF)⁴ of the three source parameters q_i , η_S^i and α_i (where i is either p or He). The three data sets on which we base the analysis are AMS-01, BESS98 and BESS-TeV (see Sect. 3).

PDF of α_{p} , α_{He} , and $\alpha_{\text{He}} - \alpha_{\text{p}}$. The two left panels of Fig. 5 show the PDF of α_{p} (hatched histograms) and α_{He} (empty histograms), whereas the two right panels show the PDF of $\alpha_{\text{He}} - \alpha_{\text{p}}$ to visually inspect any discrepant spectral index for the two species. For AMS-data (solid black lines), both Model II (reacceleration, $\delta = 0.23$) and Model III (reacceleration and convection, $\delta = 0.86$) show a very good agreement between their p and He spectral index, with respectively $\alpha_{\text{II}} \approx 2.45$ and $\alpha_{\text{III}} \approx 2.3$. There are significant differences for BESS98 (red dashed lines) and BESS-TeV (blue dash-dotted lines) data: first, the match between α_{He} and α_{p} is not as good as for AMS-01, yet $\alpha_{\text{He}} - \alpha_{\text{p}}$ remains marginally consistent with 0. The plots on the right panels and the width of the PDF tell us that the data current precision does not allow to separate differences $\lesssim 0.1$ in the spectral indices.

⁴ The MCMC technique and the interface with the propagation code is explained in details in Putze et al. (2009). A shorter introduction is given in Putze et al. (2010).

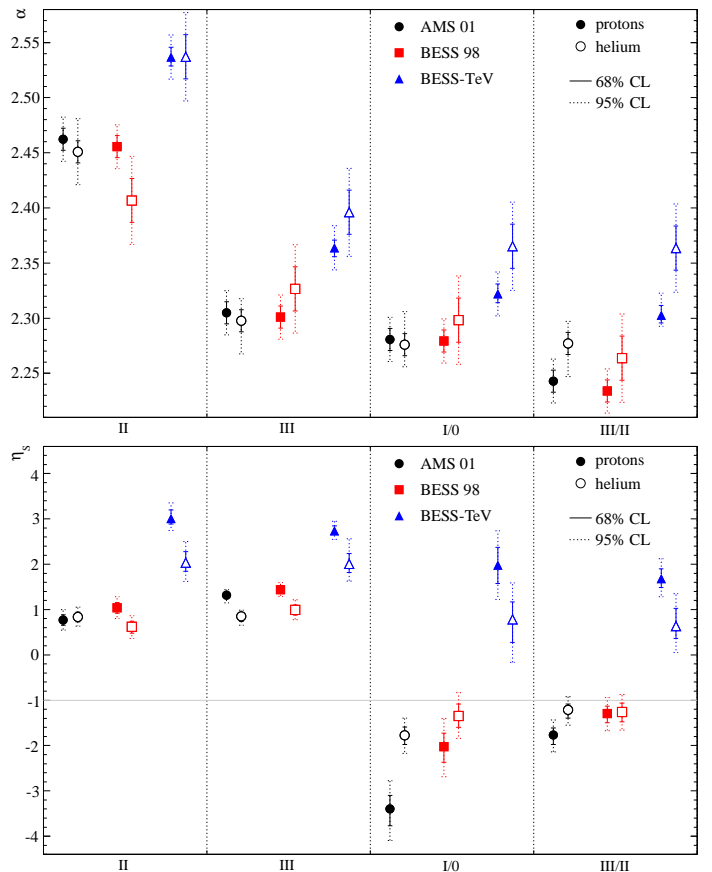


Fig. 6. Best-fit value (symbols), 68% and 95% CIs for p (filled symbols) and He (empty symbols) for the four propagation configurations gathered in Tab. 2. Top panel: spectral index α . Bottom panel: low-energy source parameter η_S [see Eq.(4)]. The grey line $\eta_S = -1$ corresponds to the value for which the source spectrum is a pure power-law in rigidity (i.e. $dQ/d\mathcal{R} \propto \mathcal{R}^{-\alpha}$).

The 68% and 95% CIs on the spectral indices for the four transport configurations of Table 2 and the three sets of data are shown in the top panel of Fig. 6. From a quick eye inspection, the following trends are found:

- for any given data set and species (p or He), the spread in the source slopes is $\alpha_{\text{p}} - \alpha_{\text{He}} \lesssim 0.2$, regardless of the model (values in the same column in Table 3);
- for any given model, the typical spread in α when fitting different data sets (values in the same row in Table 3) is ≈ 0.05 for α_{p} and ≈ 0.1 for α_{He} . This is larger than the errors extracted from the MINUIT minimisation routine, that gives a statistical spread $\alpha_{\text{p}} - \alpha_{\text{He}} \lesssim 0.01$ (not shown);
- the spectral indices obtained from BESS-TeV data are systematically larger and slightly incompatible with those found for AMS-01 and BESS98. This may be related to the systematically higher value obtained for η_S (see below).
- model II (reacceleration only) gives larger spectral indices, inconsistent with the values found for the three other models. This is not unexpected as it has the smallest δ of all models (considered in Table 2).

Table 3. Best-fit spectral index α for p and He fit and associated $\chi^2_{\min}/\text{d.o.f.}$ (models/data correspond to those shown in Fig. 5, and the number of data for the fit is roughly the same for each species).

Model/Data	AMS-01	BESS98	BESS-TeV
	α^{best}	$\chi^2_{\min}/\text{d.o.f.}$...
— Protons —			
II	2.46	2.14	2.45
III	2.30	3.72	2.30
III/II	2.24	2.05	2.23
I/0	2.28	0.14	2.28
	0.70	2.54	0.48
	1.75	2.36	2.07
	0.73	2.30	0.93
	0.18	2.32	0.56
— Helium —			
II	2.45	3.54	2.41
III	2.30	2.85	2.32
III/II	2.27	2.02	2.26
I/0	2.27	1.00	2.30
	0.69	2.53	0.34
	0.41	2.39	0.40
	0.33	2.36	0.25
	0.21	2.36	0.24

A scatter of ~ 0.2 is thus attributed to the fact that we do not know which model is best, and a scatter ~ 0.1 because of systematics in the data.

Low energy and confidence intervals (CIs) on η_S The 68% and 95% CIs on the parameter η_S controlling the low-energy behaviour of the source spectrum⁵ are shown for the same models/data in the bottom panel of Fig. 6. BESS-TeV data being at slightly higher energy than AMS-01 and BESS98, its source spectrum low-energy parameter η_S is less constrained. Otherwise, the p and He η_S point to fairly similar values for any given propagation configuration. However, this value depends on the model chosen: the reacceleration model (II) and convection/reacceleration model (III) both favour $\eta_S \approx 1$, whereas η_S is close to -2 for Model I/0 and -1.5 for Model III/II. The latter value is consistent with a source spectrum being a pure power-law in rigidity, whereas the former value implies a flattening at low energy. This is understood if we inspect the quantity $\eta_S - \eta_T$, appearing in Eq. (8): for models II and III that have $\eta_T = 1$, this give $\eta_S - \eta_T \approx 0$. For models I/0 and III/II that have respectively $\eta_T = -2.6$ and -1.3 , this gives $\eta_S - \eta_T \approx 0.6$ and -0.2 . So it seems that the constraint $\eta_S - \eta_T \approx 0$ should be met for any propagation model.

Source abundances q_i The scatter is quite large when all the different models/data are considered. The absolute values are not meaningful since they depends on the choice of L that is arbitrary set to 4 kpc in this analysis. We nevertheless note that the ratio $q_{\text{He}}/q_{\text{p}}$ falls in the range 0.3-0.6 (not shown), with a typical spread of $\approx 0.1 - 0.2$ for the PDF.

Spectra, goodness of fit, and high-energy asymptotic regime The data along with the best-fit spectra for all models are shown in Fig. 7. An eye inspection shows a good match to the data. More precisely, the $\chi^2_{\min}/\text{d.o.f.}$ values given in

⁵ We underline that for IS fluxes, the lowest energy data points are at ~ 0.8 GeV/n for p and ~ 0.4 GeV/n for He, see Fig. 2. This corresponds to $\beta_{\text{p}} \sim 0.8$ ($\beta_{\text{He}} \sim 0.7$), so that having a pre-factor β^3 amounts to a difference of $\sim 1/2$ ($\sim 1/3$ for He) with respect to the case $\eta_S = 0$ for this low energy point.

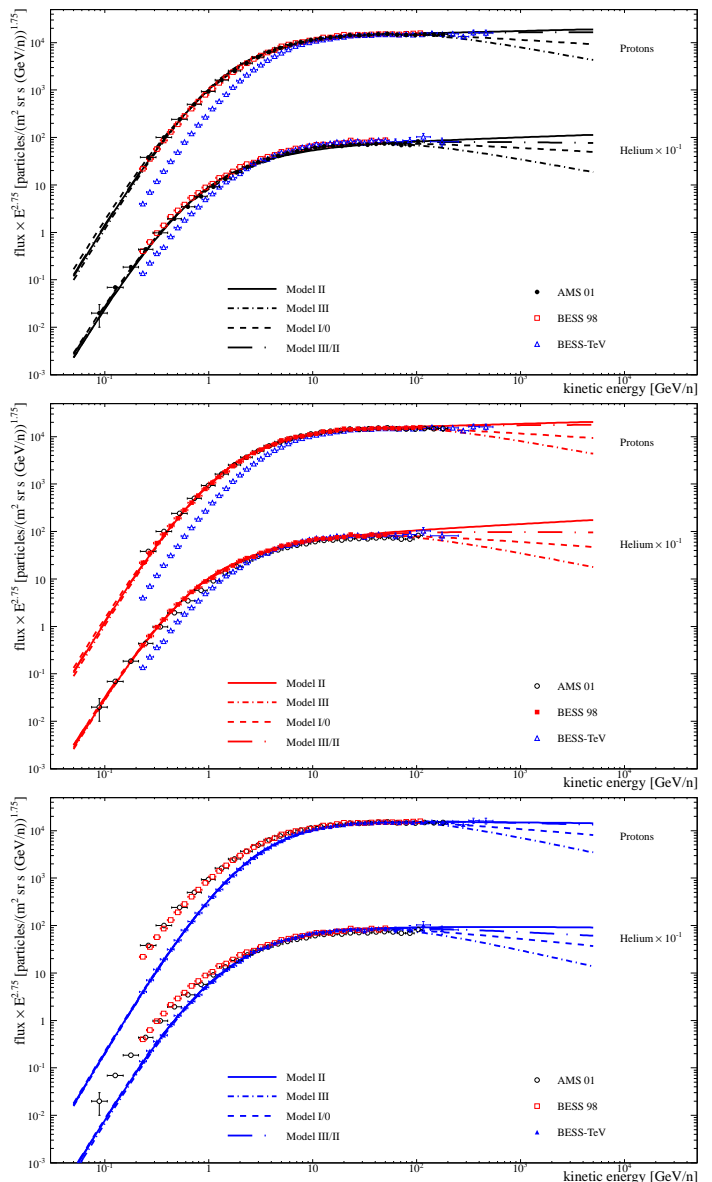


Fig. 7. TOA (modulated) fluxes (times $E_{k/n}^{2.75}$) as a function of the kinetic energy per nucleon, for p and He. The symbols are black circles for AMS-01, red squares for BESS-98, and blue triangles for BESS-TeV. The curves correspond (for the four models of Table 2) to the best-fit spectra obtained by a fit on the AMS-01 data (top panel), BESS98 data (middle panel) and BESS-TeV data (bottom panel).

Table 3 tell us that the fit to the data is very good for BESS98 and BESS-TeV, but not satisfactory for most of the models with AMS-01 data (for which the first and last two bins are not well reproduced given their small error bars). We remark that the spread in δ is larger than the spread in α (see above). Hence, the smaller δ , the smaller $\gamma_{\text{asympt}} (= \alpha + \delta)$. This is consistent with the same ordering for all species of the propagated spectra—from larger to smaller γ_{asympt} —seen on Fig. 7. The top curve is always Model II ($\delta = 0.23$, solid lines), going down to Model III/II ($\delta = 0.51$, long dash-dotted lines), Model I/0 ($\delta = 0.61$, dashed lines), and then Model III ($\delta = 0.86$, short dash-dotted lines) for the bottom curve. This emphasises that

more accurate data in the high energy regime (TeV-PeV) are needed to better constrain the asymptotic behaviour.

Envelopes on IS fluxes and consistency with low-energy Voyager data Finally, the three panels of Fig. 8 shows the envelopes on the IS fluxes (obtained from the 95% CIs on the parameters). The flux is extrapolated down to an IS energy of ~ 0.1 GeV/n, where the demodulated Voyager energies fall (Webber & Higbie 2009)⁶. On the same plots are shown the demodulated AMS-01, BESS98, BESS-TeV, and Voyager data. The extrapolation of the curvatures of the AMS-01 and BESS98 data at Voyager energies are hardly consistent with each other. BESS-TeV data look better in that respect. The data for He, falls nicely into place. This is possibly related to the use of the force-field approximation that is known to fail for the very low-energy protons (Perko 1987). For the envelopes based on BESS-TeV data (right panel), almost all models are allowed, except perhaps model III (standard diffusion with convection and reacceleration). On the other hand, from the envelopes from AMS-01 and BESS98 data, the modified diffusion scheme models (I/0 and III/II) are disfavoured by Voyager data (that were not included in the fit). Again, it is difficult to conclude given the inconsistencies between the various data sets, but such plots clearly show the potential of future analysis to access the low-energy source spectrum (using Voyager data closer to the IS state and/or more accurate low-energy data from PAMELA and AMS-02).

4.2.3. Summary

An important result of the analysis presented in the previous Section is that, independently of the model and data considered, the source slope of p and He nuclei is constrained to fall in the range 2.2 – 2.5 (or 2.2 – 2.4 if we discard Model II). As the range of δ covered by these models falls in the range 0.23–0.86 (see Table 2), this is a robust prediction. It also means that the asymptotic value for the propagated spectra ($\gamma_{\text{asympt.}} \equiv \alpha + \delta$), that falls in the range 2.7 – 3.0, is not reached in the GeV/n to TeV/n regime (as direct fits to the nuclei at $E_{k/n} > 100$ GeV/n propagated spectra lead to $\gamma_{\text{data}} \approx 2.65$, Ave et al. 2008): residual propagation effects (reacceleration, convection, spallations) are still active.

Another important result is that regardless of the propagation model used, the quantity $\eta_S - \eta_T$ is constrained to be ~ 0 . Hence, to reproduce the data, if a pure power-law rigidity spectrum is assumed, a *non-standard* low-energy diffusion coefficient (upturn at low energy) is required. Conversely, if a *standard* diffusion coefficient is assumed (i.e. $K(E) = K_0 \beta \mathcal{R}^\delta$), a flattening of the low-energy source spectrum is required (i.e. $dQ/dR \propto \beta^{\eta_S+1} \mathcal{R}^{-\alpha}$ with $\eta_S > -1$). The close-to-IS condition low-energy Voyager data is a further piece of information to break the degeneracy $\eta_S - \eta_T$, and would possibly provide the shape of the low-energy source spectrum.

⁶ The estimated modulation parameter is 60 MV for these data (Webber & Higbie 2009).

4.3. Constraints on heavier primary species

4.3.1. Preamble

Heavier primary species (from C to Fe) are less abundant and thus more difficult to measure than p and He. As a result, the spread in their measurement and their error bars are larger than those for the p and He fluxes. But they still provide some useful information. Indeed, the heavier the species, the larger its destructive rate. Hence, the universality of the source spectrum can be checked against the above effect (which is species dependant).

Below, we repeat the analysis performed on p and He for the C, O, Ne, Mg, Si, S, Ar, Ca and Fe elements. These elements are almost all completely dominated by the primary contribution, except for S and Ar that receive a $\sim 20\%$ secondary contribution. To speed up the calculation, but still take into account this contribution, we separate the nuclei to propagate in three families: ^{12}C – ^{30}Si , ^{32}S – ^{48}Ca , and ^{54}Fe – ^{64}Ni .

Such a study complements and extends the analysis performed by the HEAO-3 group (Engelmann et al. 1990), the Ulysses group (Duvernois & Thayer 1996), and the TRACER group (Ave et al. 2009), in which only one propagation model, a universal source spectral index α for all species, and a single experiment was considered. Below, α_i , q_i and η_S^i are free parameters for each primary species, which allows us to i) test the universality of the source spectra, ii) take into account the correlations between the normalisation q_i and the spectral index α_i (Putze et al. 2009), and iii) inspect the systematic spread on the source parameters as several configurations of the diffusion model are taken. The goal is to get more robust results (as more potential sources of uncertainties are taken into account). Besides, the MCMC technique is again helpful in providing a sound statistical estimate of the error bars on the source parameters.

We restrict our analysis to the HEAO-3 (Engelmann et al. 1990), TRACER (Ave et al. 2008) and CREAM-II (Ahn et al. 2009) data, to keep only the data covering as large as possible an energy region, and also to avoid very low-energy data that are more sensitive to solar modulation.

4.3.2. Results

We first show the fit to the data in Figs. 9, 10, and 11. They all show the same sets of data, but each figure corresponds to a fit to a single experiment (respectively, HEAO-3, CREAM-II and TRACER). Note that each species has three free parameters α (slope), q (normalisation), and η_S (low-energy behaviour).

Fit to HEAO-3 data In Fig. 9 (i.e. fit to HEAO-3), the four propagation configurations of Table 2 lead to the same shape at low energy. This is not surprising since this is where the bulk of HEAO-3 data lies. The high-energy asymptotic behaviour is then influenced by the value of the diffusion slope δ , as is the case for p and He. Similarly, the spread in δ is larger than the spread in α (see below). It means that the smaller δ , the smaller $\gamma_{\text{asympt}} = \alpha + \delta$, so the same ordering according to the γ_{asympt} value of the model is seen at high energy: Model II on top (largest γ_{asympt}), then Model III and I/0, and Model III/II at bottom. An

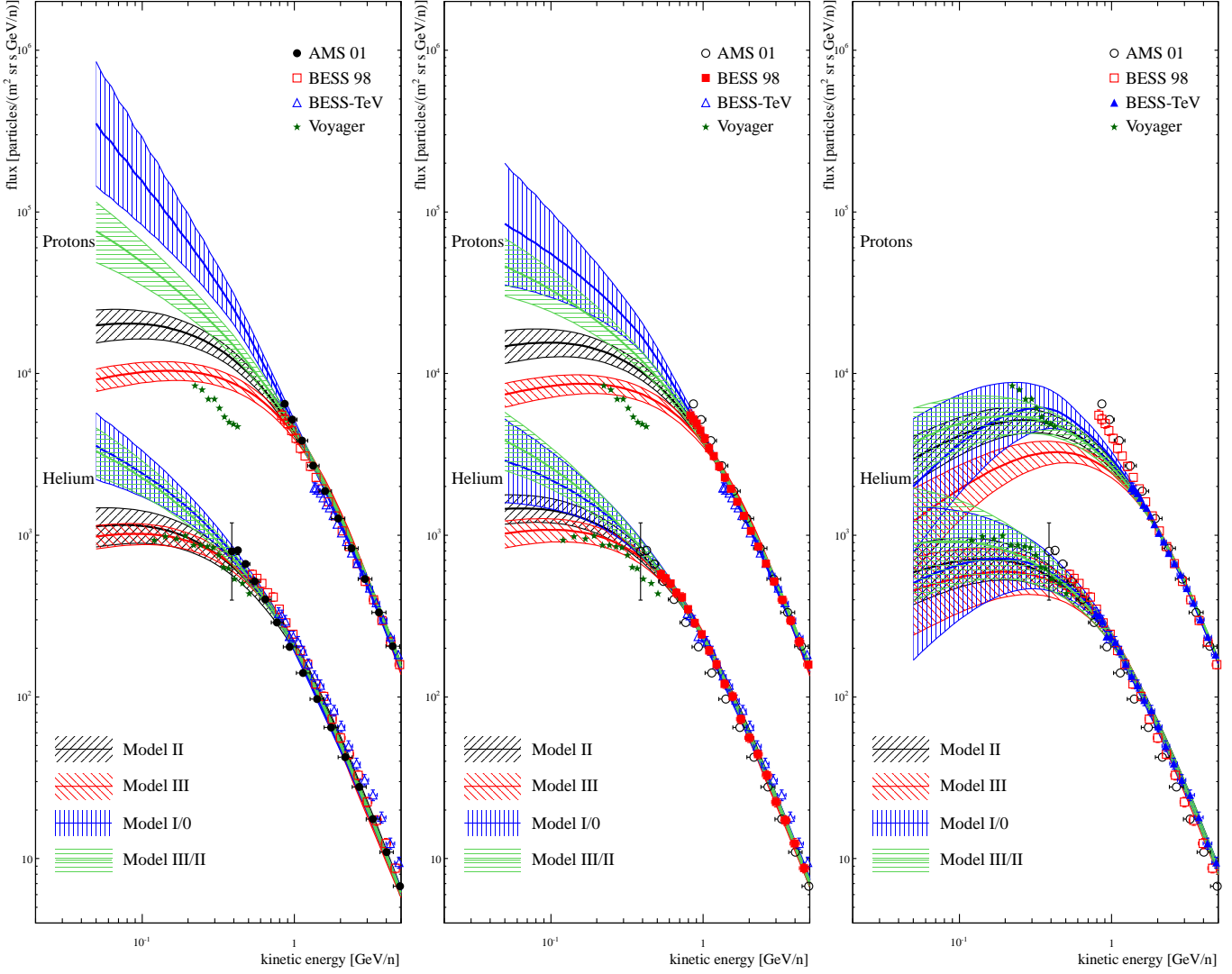


Fig. 8. 95% CL envelopes for the proton and helium fluxes for the four propagation configurations of models of Table 2. The three panels correspond respectively to the result of the MCMC analysis on AMS-01 data (left panel), BESS98 data (middle panel), and BESS-TeV (right panel). For the sake of comparison, the IS (demodulated) AMS-01 (black circles), BESS98 (red squares), BESS-TeV (blue triangles), along with the Voyager data (stars).

eye inspection shows that Model I/0 and Model III/II are the ones in best agreement with the higher energy data (CREAM-II and TRACER).

Fit to CREAM-II and TRACER data Fig. 10 shows the resulting best-fit spectra for the same models, but now fitted on CREAM-II data only. The data being at higher energy, the parameter η_S is unconstrained and we set it to -1 for this fit only. Unsurprisingly, most models are not able to match the lower-energy HEAO-3 data. For the lighter species, $\alpha + \delta$ remains the same, regardless of the model. The CREAM-II data for these species are $\gtrsim 100$ GeV/n, in a regime where the asymptotic slope γ_{asympt} is reached. For the heavier species, where the data go down to a few tens of GeV/n, a similar ordering (yet less clear) of the models with γ_{asympt} (as for the HEAO-3 fit) is seen for the high-energy asymptotic behaviour. The fits to TRACER data shown in Fig. 11 are just in-between. Indeed, the energy range covers the same energy range as CREAM-II, but a few data point

at low energy force the spectrum to bend. However, there is a gap between the two energy regimes, where the curvature of the HEAO-3 data is not reproduced⁷.

Goodness of fit Table 4 shows the best-fit spectral index α_i and the associated $\chi^2_{\text{min/d.o.f.}}$ value for the various models, species, and data sets. Unsurprisingly, the best-fit (smaller $\chi^2_{\text{min/d.o.f.}}$ value) are for the CREAM-II data that only cover the high energy range. It is indeed more difficult to reproduce the low energy part, where data have smaller error bars, but also where more effects (modulation, continuous and catastrophic losses) shape the spectrum. For the HEAO-3 case, the $\chi^2_{\text{min/d.o.f.}}$ value is large for most of

⁷ Model I/0 is not used on these data because it leads to unphysical values. This is likely to be related to the unphysical large negative value of η_S required, that becomes an issue for the numerical inversion of the energy losses (no convection and reacceleration to smooth out the steep upturn in the low-energy spectrum here, at variance with the three other models).

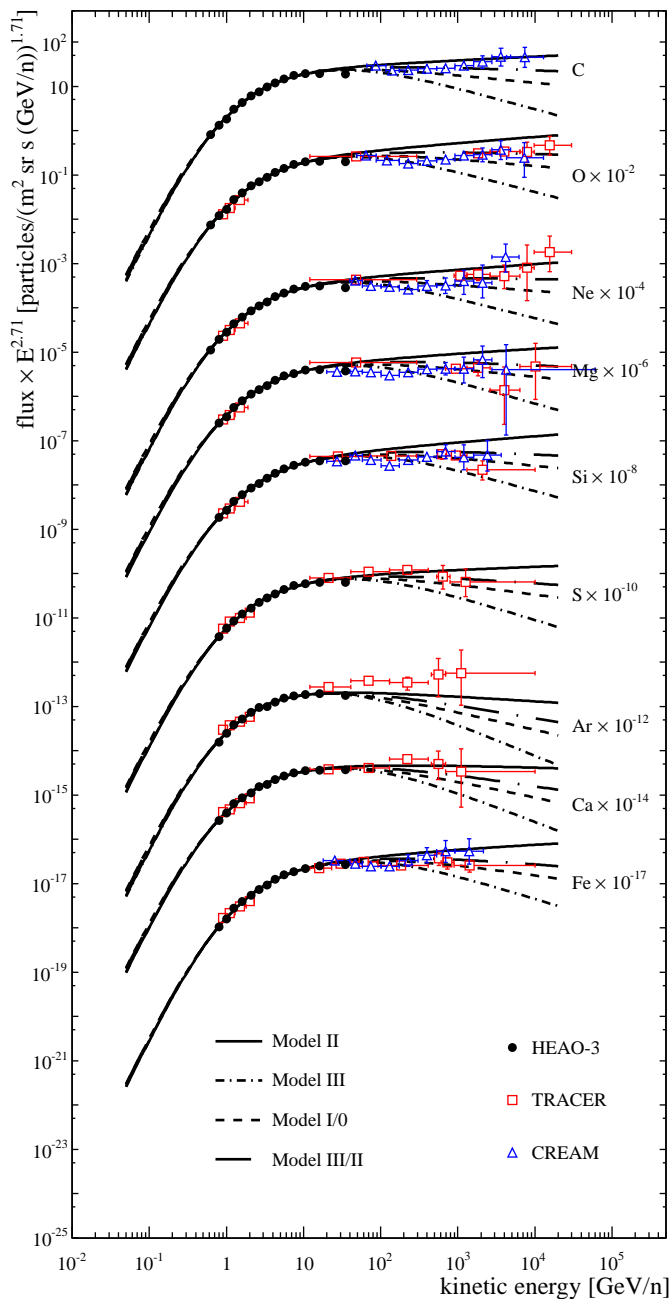


Fig. 9. TOA (modulated) fluxes (times $E_{k/n}^{2.71}$) as a function of the kinetic energy per nucleon, for primary species from C to Fe. The symbols are black circles for HEAO-3 (Engelmann et al. 1990), red squares for TRACER (Ave et al. 2008) and blue triangles for CREAM-II (Ahn et al. 2009). The curves correspond (for the four models of Table 2) to the best-fit spectra obtained by a fit on the HEAO-3 data only.

the species because of the difficulty to fit the highest energy point that has a very small error bar. For S, Ar and Ca, the fit is better. Data from the next CREAM flights, or from the AMS instrument should help clarify the situation, and confirm or infirm these discrepancies amongst the various data. Nevertheless, some conclusions can still be drawn on the spectral indices (see below), although they are less constraining than those derived from the p and He data.

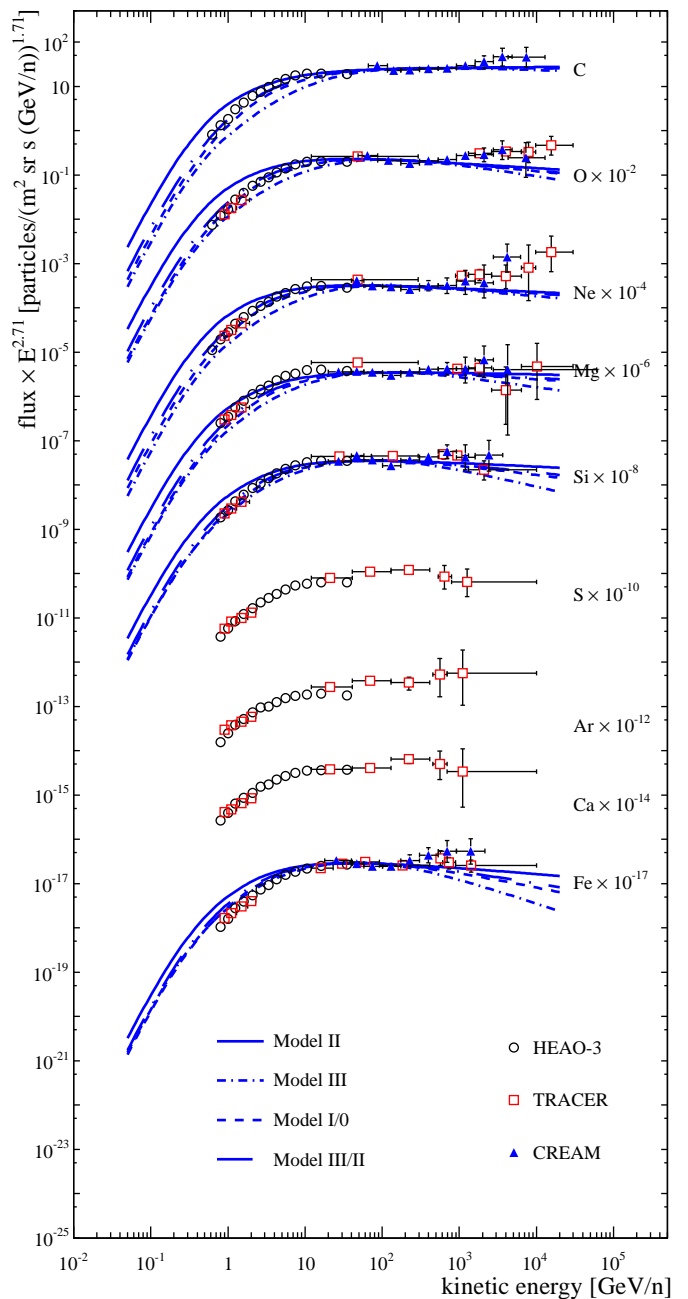


Fig. 10. Same as in Fig. 9, but the source spectra are now fitted on the CREAM-II data only (no published data for S, Ar, and Ca).

Confidence intervals on α , q and η_S Figure 12 shows, along with the 68% and 95% CIs, the best-fit values on the spectral indices α_i (top panel), the relative source abundances q_i (middle panel), and the source parameter η_S^2 , for all the primary species considered in this study. We first underline that the 95% CL relative uncertainty for the parameters ranges from $\lesssim 5\%$ on α_i and $\lesssim 20\%$ on q_i . CREAM data cover a too narrow energy range to give stringent constraints, so we do not comment on them further below. The following trends are observed for the parameters:

- α (top panel): as for the p and He data, Model II (reacceleration only, filled circle) always gives a larger value than the other models. Moreover, a similar range of

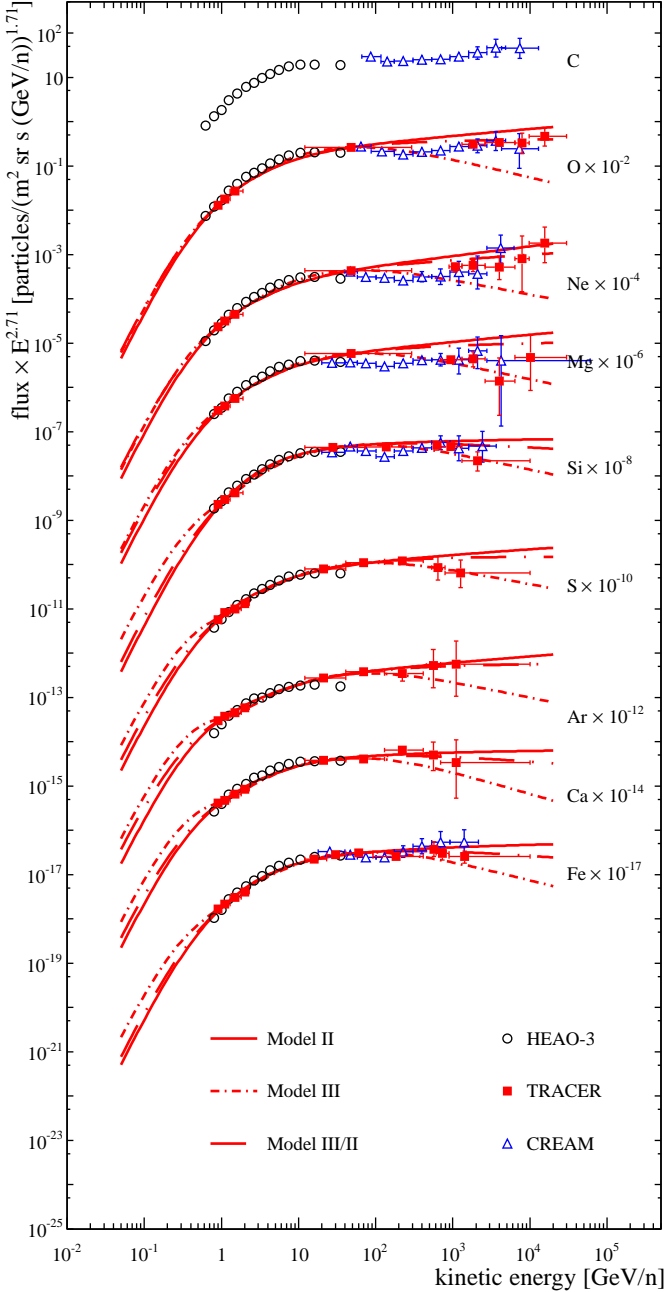


Fig. 11. Same as in Fig. 9, but the source spectra are now fitted on the TRACER data only.

slopes is found (2.2 – 2.5 for HEAO-3 data only, but more scatter when using TRACER data).

- q_i (middle panel): the relative abundances from HEAO-3 data are quite insensitive to the propagation model used. We recover the values of Engelmann et al. (1990) (green boxes), although with larger error bars. The discrepancy for S, Ar and Ca (our values are larger than those of the HEAO-3 analysis) is probably related to the fact that for the latter the highest energy data point is better fitted than for the others (see above): this results in a larger value of η_S and α that may be responsible for the difference observed on the q_i . The relative abundances obtained from the TRACER data are sensitive to the model chosen, presumably because of the lack of constraints in the intermediate energy range.

Table 4. Best-fit spectral index α and associated $\chi^2_{\min}/d.o.f.$ for the fit of the source spectrum parameters. Each column correspond to a different set of data on which the fit is performed.

Model	HEAO-3	TRACER		CREAM		
	α_{best}	$\frac{\chi^2_{\min}}{d.o.f.}$	
— Carbon —						
II	2.41	7.16	N/A	N/A	2.48	1.59
III	2.33	6.14	N/A	N/A	1.90	2.15
I/0	2.28	5.96	N/A	N/A	2.11	1.78
III/II	2.27	6.54	N/A	N/A	2.21	1.73
— Oxygen —						
II	2.37	7.34	2.35	15.17	2.61	3.17
III	2.32	6.11	2.27	13.76	2.18	4.59
I/0	2.26	6.08	N/A	N/A	2.28	3.69
III/II	2.26	6.61	2.19	2.54	2.37	3.54
— Neon —						
II	2.37	3.94	2.27	5.59	2.57	0.85
III	2.30	2.85	2.19	3.06	2.01	1.09
I/0	2.24	3.54	N/A	N/A	2.21	0.93
III/II	2.23	3.80	2.09	1.68	2.31	0.91
— Magnesium —						
II	2.40	7.13	2.35	26.79	2.54	0.69
III	2.35	6.03	2.23	0.60	2.10	1.28
I/0	2.29	6.37	N/A	N/A	2.22	0.90
III/II	2.29	6.79	2.17	11.47	2.31	0.83
— Silicon —						
II	2.38	3.95	2.49	53.88	2.60	2.08
III	2.34	3.15	2.24	3.89	2.25	2.93
I/0	2.29	3.35	N/A	N/A	2.33	2.41
III/II	2.29	3.63	2.31	35.14	2.40	2.30
— Sulfur —						
II	2.44	1.79	2.39	2.22	N/A	N/A
III	2.39	1.27	2.19	0.70	N/A	N/A
I/0	2.34	1.39	N/A	N/A	N/A	N/A
III/II	2.33	1.58	2.21	1.35	N/A	N/A
— Argon —						
II	2.61	1.31	2.37	0.51	N/A	N/A
III	2.57	1.18	2.22	0.62	N/A	N/A
I/0	2.51	1.26	N/A	N/A	N/A	N/A
III/II	2.50	1.31	2.19	0.29	N/A	N/A
— Calcium —						
II	2.56	1.94	2.49	0.83	N/A	N/A
III	2.52	1.76	2.36	1.08	N/A	N/A
I/0	2.48	1.84	N/A	N/A	N/A	N/A
III/II	2.48	1.90	2.34	0.73	N/A	N/A
— Iron —						
II	2.43	4.05	2.48	19.60	2.67	1.54
III	2.39	3.77	2.29	2.48	2.42	2.37
I/0	2.36	3.88	N/A	N/A	2.46	1.94
III/II	2.35	3.98	2.34	11.95	2.52	1.80

- η_S (bottom panel): as for the p and He data, a trend is observed for the dependence on the models. The pattern is the same, but with the value of η_S one larger than that for p and He. In terms of $\eta_S - \eta_T$, the C to Si primary species favours ≈ 1 , whereas p and He data favour ≈ 0 . There is more scatter in the S to Fe data, but we remind that the HEAO-3 data are based on different use of sub-detectors to get this heavier species.

Summary. The conclusions are quite similar and even reinforce those obtained from the p and He analysis. First, all

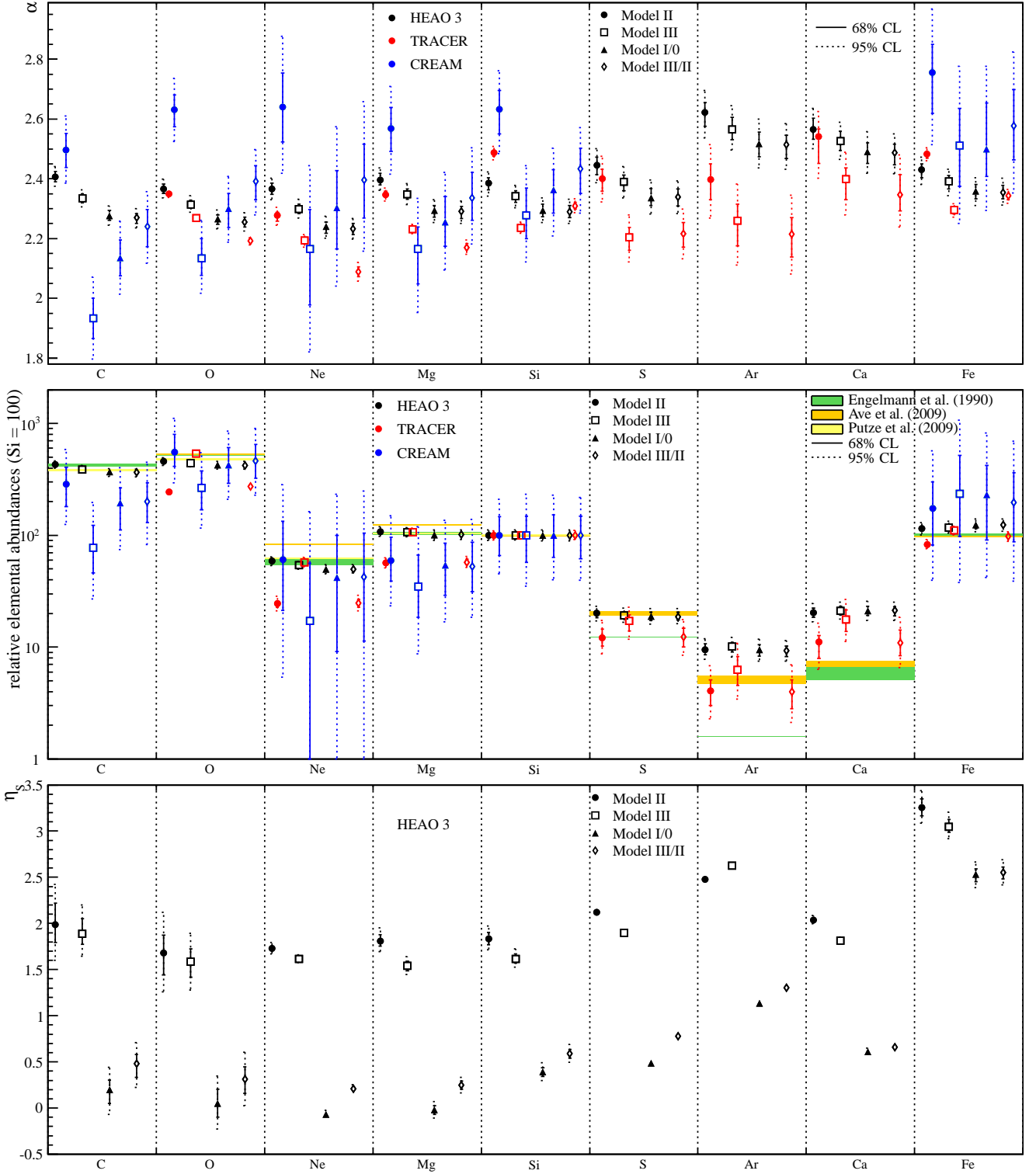


Fig. 12. Best-fit value (symbols), 68% (dashed error bars) and 95% (solid error bars) CLs for C to Fe source parameters from the fit on CREAM-II, HEAO-3, and TRACER data. Top panel: source spectral index α_i . Middle panel: relative abundances q_i . The results from the analysis of the HEAO-3 group (Engelmann et al. 1990) are shown as green boxes, and those from the TRACER group (Ave et al. 2009) as orange boxes. The yellow boxes correspond to a leaky-box analysis of the abundances on HEAO-3 data performed in Putze et al. (2009). Bottom panel: low-energy source parameter η_S [see Eq.(4)]. Only the results from HEAO-3 data are plotted (for CREAM-II, η_S is set to -1, and for TRACER, the scatter is so large that the values are meaningless).

primary species favour a source slope in the range 2.2 – 2.5, regardless of the propagation configuration used. The quantity $\eta_S - \eta_T$ is also constrained from C to Fe primary data,

but whereas $\eta_S - \eta_T \approx 0$ for p and He, we get $\eta_S - \eta_T \approx 1$ for the heavier nuclei. It is unclear whether this effect should be attributed in a difference of the low-energy source spectra,

or if it is just the result of a systematic bias in the solar modulation level, or of systematics in the data. Finally, most of the derived relative source abundances are in agreement with those derived by earlier groups. Still, there are a few differences. A slight dependence on the propagation configuration is also observed. Due to the relevance of the value of the source abundances in the context of acceleration mechanisms (Dwyer & Meyer 1987; Meyer et al. 1997; Ellison et al. 1997; Ogliore et al. 2009), this point deserves further investigation.

5. Ratio of primary species

Webber & Lezniak (1974), more than 30 years ago, recognised the importance of looking at primary ratios. Such ratios may be, in principle, used to i) check the consistency of spectral indices of various species, ii) inspect whether source spectra are power-law in rigidity or power-law in kinetic energy, and also iii) inspect whether solar modulation is a rigidity or total energy effect. Below, we present several plots to illustrate some of these ideas, but also underline the complications that arise due to the many degeneracies between the source, transport, and modulation parameters (as underlined in the previous sections).

5.1. p/He ratio

Concerning the p/He ratio⁸ on which Webber & Lezniak (1974) study mainly focused, the main conclusions were: i) proton and helium source spectra are rigidity rather than energy/nucleon spectra, ii) modulation effects dominate the shape of the p/He ratio for such rigidity spectra when shown as a function of kinetic energy, and iii) modulation effects is not a pure rigidity effect since it flattens the spectrum at low energy.

p/He from the toy-model calculation Caution is in order when calculating the ratio p/He, whether we start from the differential flux in energy or in rigidity. In an analogous manner as for Eq. (3),

$$\psi_{E_{k/n}}(E) \equiv \frac{d\psi}{dE_{k/n}}$$

and

$$\psi_{\mathcal{R}}(E) \equiv \frac{d\psi}{d\mathcal{R}} = \frac{Z\beta}{A} \cdot \psi_{E_{k/n}}(E),$$

in order to define

$$\left. \frac{p}{He} \right|_{\mathcal{R}} = \frac{\psi_{\mathcal{R}}^p}{\psi_{\mathcal{R}}^{\text{He}}} = \frac{2\beta_p}{\beta_{\text{He}}} \cdot \left. \frac{p}{He} \right|_{E_{k/n}}.$$

In the 1D toy-model (energy gains and losses discarded), assuming Eq. (4) for the source term—i.e. $dQ/d\mathcal{R} = q\beta^{\eta_S+1}\mathcal{R}^{-\alpha}$ —, and Eq. (1) for the diffusion coefficient—i.e. $K(\mathcal{R}) = \beta^{\eta_T}K_0\mathcal{R}^\delta$ —, we have the analog of Eq. (7), but

⁸ Note that because of the misidentification of ³He and ⁴He, Webber & Lezniak (1974) estimate a $\lesssim 2.5\%$ effect in the data plotting the same measurement as rigidity spectra or kinetic energy spectra, that is as well not considered below.

expressed in terms of the rigidity:

$$\left. \frac{p}{He} \right|_{\mathcal{R}} = \frac{2q_p}{q_{\text{He}}} \cdot \frac{\beta_p^{\eta_S+2}(\mathcal{R})}{\beta_{\text{He}}^{\eta_S+2}(\mathcal{R})} \cdot \mathcal{R}^{-(\alpha_p-\alpha_{\text{He}})} \times \frac{\beta_{\text{He}}^{\eta_T}(\mathcal{R})}{\beta_p^{\eta_T}(\mathcal{R})} \cdot \frac{K_0\mathcal{R}^\delta/(hL) + nc \cdot \beta_{\text{He}}^{1-\eta_T}(\mathcal{R}) \cdot \sigma_{\text{He}}}{K_0\mathcal{R}^\delta/(hL) + nc \cdot \beta_p^{1-\eta_T}(\mathcal{R}) \cdot \sigma_p} \quad (9)$$

where we made explicit the rigidity dependence for all the terms (c is the speed of light). If the destruction rate is subdominant, we have

$$\left. \frac{p}{He} \right|_{\mathcal{R}} \stackrel{\sigma \rightarrow 0}{=} \frac{2q_p}{q_{\text{He}}} \cdot \frac{\beta_p^{\eta_S+2-\eta_T}(\mathcal{R})}{\beta_{\text{He}}^{\eta_S+2-\eta_T}(\mathcal{R})} \cdot \mathcal{R}^{-(\alpha_p-\alpha_{\text{He}})}. \quad (10)$$

In all the above formulae, we have

$$\beta = \frac{\mathcal{R}}{\sqrt{\mathcal{R}^2 + m^2/Z^2}} \approx \frac{\sqrt{E_{k/n}(E_{k/n} + 2)}}{E_{k/n}}$$

For a proton $m^2/Z^2 \approx 1$, whereas ≈ 4 for an Helium. This is sufficient to distort the low energy p/He ratio whenever it is calculated from the differential fluxes in rigidity and $\eta_S + 2 - \eta_T \neq 0$. However, if the ratio is calculated from the differential fluxes in kinetic energy per nucleon, for a given $E_{k/n}$, we have $\beta_p(E_{k/n}) \approx \beta_{\text{He}}(E_{k/n}) \equiv \beta$, and Eq. (9) reduces to

$$\left. \frac{p}{He} \right|_{E_{k/n}} \approx \frac{q_p}{q_{\text{He}}} \cdot \frac{[E_{k/n}(E_{k/n} + 2)]^{-(\alpha_p-\alpha_{\text{He}})/2}}{2^{-\alpha_{\text{He}}}} \times \frac{K_0[E_{k/n}(E_{k/n} + 2)]^{\delta/2}2^\delta/(hL) + nc\beta^{1-\eta_T}\sigma_{\text{He}}}{K_0[E_{k/n}(E_{k/n} + 2)]^{\delta/2}/(hL) + nc\beta^{1-\eta_T}\sigma_p} \quad (11)$$

When the destruction rates are subdominant, we get

$$\left. \frac{p}{He} \right|_{E_{k/n}} \stackrel{\sigma \rightarrow 0}{=} \frac{q_p}{q_{\text{He}}} \cdot \frac{[E_{k/n}(E_{k/n} + 2)]^{-(\alpha_p-\alpha_{\text{He}})/2}}{2^{-\alpha_{\text{He}}-\delta}}. \quad (12)$$

Comparison to data The p/He ratio is displayed as a function of the kinetic energy per nucleon in the left panel of Fig. 13, for the BESS98 (red squares) and BESS-TeV (blue circles) data. The solid lines (no inelastic reaction terms) result from Eq. (12), with $\alpha_p = \alpha_{\text{He}}$. The shape of the ratio as well as the differences between the data taken at two different solar periods can be almost completely ascribed to the modulation effect. The effect of the inelastic reaction term is contained in Eq. (11). A closer look to this equation shows that the numerator and the denominator do not differ by at most a factor of ~ 3 , confirming the subdominant (though important) role of this effect to shape the ratio (displayed versus kinetic energy per nucleon). The effects (not shown) of having different spectral indices for p and He, having different values of α , δ , and $\eta_S - \eta_T$, when varied within reason, is of the same amount as the effect of the destruction rate. But these effects are better seen when working with the rigidity.

The right panel of Fig. 13 shows a few experiments that have provided the p/He ratio as a function of the rigidity. Except for ATIC-1, the error bars are not reproduced, but are expected to be of the order of the size of the symbols⁹.

⁹ The AMS-01 p and He flux given in AMS Collaboration et al. (2002) are not calculated for the

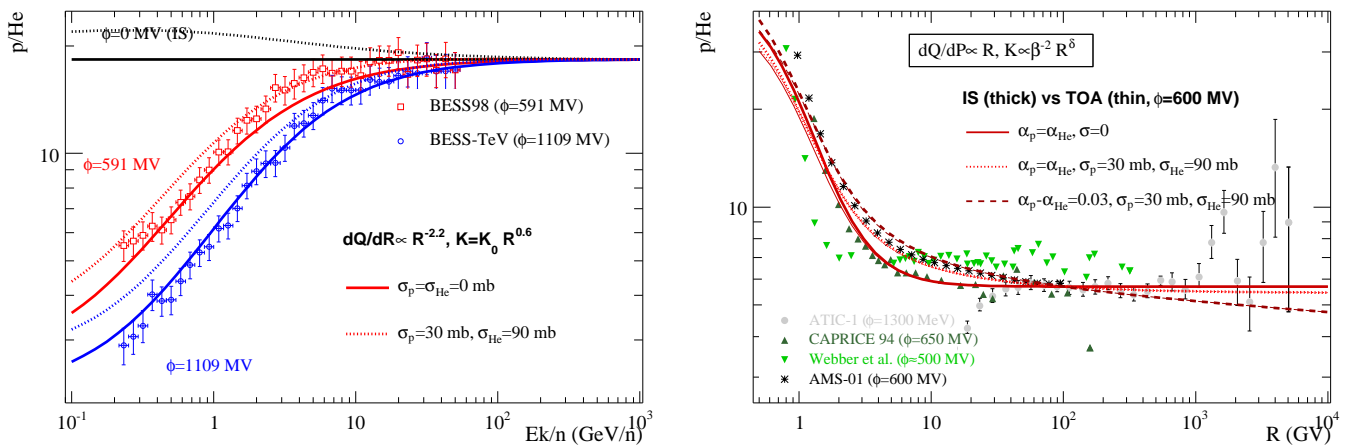


Fig. 13. Left panel: p/He ratio as a function of E_k/n , along with BESS98 (Sanuki et al. 2000) and BESS-TeV (Haino et al. 2004) data. The lines show the toy-model calculation without the destruction term (thick solid lines) and with it (thick dotted lines). The black, red and blue lines are respectively modulated to $\Phi = 0$ MV (IS), $\Phi = 591$ MV and $\Phi = 1109$ MV. Left panel: same ratio, but as a function of the rigidity. The data are AMS-01 (AMS Collaboration et al. 2002), ATIC (Zatsepin et al. 2003), CAPRICE 94 (Boezio et al. 1999), and some balloon data (Webber et al. 1987). The three toy-model calculations corresponds to the destruction rate set to zero (solid lines) or to its required value (dotted lines), plus a difference in the spectral index of p and He (dashed lines). In both plots, the normalisation is arbitrarily set to match the data.

As underlined in the previous sections, even though all experiments claim small error bars, not many of them are consistent with each other for the p and He fluxes. On the other hand, one would expect the ratio to have less systematics than fluxes. Yet, a large discrepancy remains (that cannot be explained by the different level of solar modulation associated to each experiment). The various curves show: i) the effect of solar modulation is sub-dominant for p/He vs \mathcal{R} (thick vs thin lines); ii) the effect of inelastic interactions, which are switched off (solid lines) or included (dotted lines); iii) the ratio distortion due to a possible difference in the spectral indices of p and He (dashed lines). The shape of the ratio depends mostly on the value of $\eta_S - \eta_T$. As found in Eq. (10), the ratio is constant if $\eta_S - \eta_T = -2$ (not shown on the figure). The best-fit to the data is obtained for $\eta_S - \eta_T \approx 1$, in gross agreement with the results of the more complete analysis of Sect. 4.2. The difference may result from the effect of energy losses that is not implemented in the toy formula. A shift of p and He spectral index is also not supported by the ratio data, in agreement with the direct fits to p and He fluxes (Sect. 4.2).

5.2. Ratio relative to the Oxygen flux

A similar analysis can be carried out for ratios of heavier species ($Z > 2$). In that case, for any element, we have $A/Z \sim 2$, so that for a given kinetic energy per nucleon, the rigidity or the β is the same for any element. The toy-model formulae is very similar to the p/He Eq. (11): the parameter η_S and η_T , as well as the solar modulation effect

same rigidity binning. We thus fitted both fluxes (expressed as a function of the nucleus rigidity) with a simple polynomial function, and calculated the ratio from these fits (shown as stars approximately along the same binning as the original He data AMS Collaboration et al. 2000). Calculating correctly the associated error bars is not straightforward: as the data are just used for eye comparison, we do not go into more details.

are not expected to be important. This is shown in the top panel of Fig. 14, for a few elements: the main ingredient shaping the X/O ratios is the inelastic scattering on the ISM.

There is a fair agreement with the data for C/O (black), Si/O (orange) and Fe/O (magenta) as shown on the right panel of Fig. 14, especially at low-energy with the ACE data (George et al. 2009). The discrepancy with Ne/O and Mg/O is only at the level of $\sim 20\%$. It could be some systematics in the data, but it deserves further investigation, especially because some isotopic anomalies in the Ne (and less likely for Mg) could be a signature for a contribution of the Wolf-Rayet stars to the standard cosmic-ray abundances (Gupta & Webber 1989; Webber et al. 1997). Such anomalies (Binns et al. 2005, 2008) could be associated with anomalies in the ratio of elements, especially if the source spectra for different accelerators are slightly different.

5.3. Summary

Up to first order, the shape of the p/He ratios, when plotted as a function of the kinetic energy per nucleon, is driven by the modulation effect. It could be used to monitor the modulation level at different periods. On the other hand, the same ratio plotted as a function of the rigidity minimises the effect of the modulation, and is well adapted to probe the values of $\eta_S - \eta_T$, and $\alpha_p - \alpha_{\text{He}}$. A full analysis using energy gains and losses is required to push further such an approach, which is complementary to the direct fit of the p and He fluxes, and that may suffer less from systematics in the data.

For X/O ratios, where X is an primary element with $Z > 2$, the behaviour as a function of E_k/n is driven by the destruction rate on the ISM. Isotopic anomalies and/or non-universality of the source slopes can be inspected by means of these ratios.

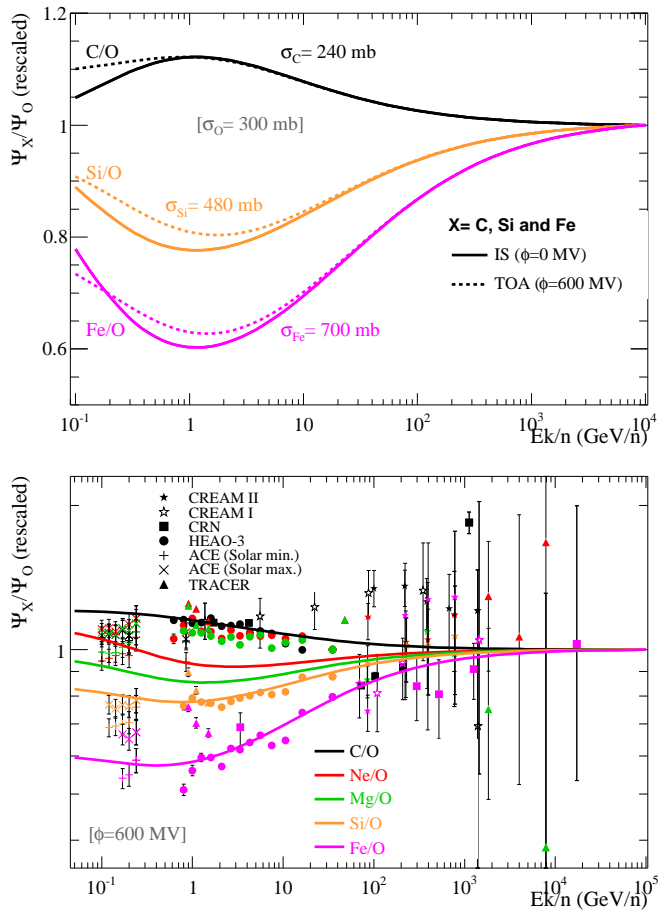


Fig. 14. Ratio of element to O as a function of the kinetic energy per nucleon. Top panel: C/O, Si/O and Fe/O without (IS, solid lines) or with (TOA, dashed lines) solar modulation. The destruction cross-section is indicated for each element. Bottom panel: comparison of the simple toy-model formula (thick solid lines) with the data (symbols): CREAM I and II (Ahn et al. 2008, 2010a,b), CRN (Swordy et al. 1990; Mueller et al. 1991), HEAO-3 (Engelmann et al. 1990), TRACER (Ave et al. 2008, 2009), and low-energy ACE data (George et al. 2009).

6. Conclusions

We have analysed the fluxes of primary cosmic rays in diffusion models with particular attention to p and He and exploring possible constraints from C to Fe data. We also present a study on the primary-to-primary ratio. The most recent data on p and He are well reproduced by a purely diffusive model, described by power law source spectrum, isotropic diffusion coefficient, spallative destructions and electromagnetic energy losses. This conclusion holds for single data sets but it is not reached in combined analysis (except for AMS01 and BESS98 proton data), due to the mean level of consistency among the different data collections. The inspection of low energy (≤ 100 GeV/n) p and He data indicates that the purely diffusive regime is likely not reached due to the role of spallations and, to less extent, of energy losses. The data are shown to be compatible with a wide class of purely diffusive models, but can also be accommodated by models with convection and/or acceleration. In all scenarios, they do not put significant constraints

on the transport parameters and tend to favour values for the source and transport parameters out of physical regions. We consider the possibility of low-energy deviations both in the diffusion coefficient $K(R) = K_0 \beta^{\eta_T} \mathcal{R}^\delta$ and in the acceleration spectrum $dQ/dR = q \beta^{\eta_S + 1} \mathcal{R}^{-\alpha}$. The addition of η_S or η_T to the p and He analysis does not lead to relevant constraints on the transport parameters, and seems to barely complicate the level of degeneracies between source and diffusion terms.

In Sect. 4 we have applied best-fit models previously selected from B/C data, to the propagation of light and heavier primary nuclei. The main results on p and He are: i) it is possible to accommodate these primary fluxes in diffusive models along with B/C data (very good fit on BESS data, less satisfactory on AMS ones); ii) α ranges between 2.2 and 2.5; iii) for any given data set and species the spread in the source power index is $\alpha_p - \alpha_{He} \lesssim 0.2$, regardless of the model; iv) p and He point to very similar η_S , whose values depend on the model: close to 1 for the reacceleration and convection/reacceleration models, whereas η_S is close to -2 for Model I/0 and -1.5 for Model III/II, which contain a low energy upturn in the diffusion coefficient by means of η_T . Indeed, the constraint which seems to emerge from any propagation model is on their difference: $\eta_S - \eta_T \approx 0 - 1$. We have demonstrated that a possible way to break the degeneracy $\eta_S - \eta_T$ inherent the low-energy tail is by means of the Voyager data, taken at a few hundreds of MeV/n, and in a quasi-IS regime.

We have studied heavier primary nuclei spectra, whose relevant destruction rate on the ISM increases roughly with atomic number. Therefore, they can be tested against a universal source spectral function. As for p and He, we have fitted data for C, O, Ne, Mg, Si, S, Ar, Ca and Fe within the models selected by B/C. As for light primaries, these nuclei point to α around 2.2-2.5 regardless of the propagation configuration used. The quantity $\eta_S - \eta_T$ is also constrained from C to Fe primary data to be $\eta_S - \eta_T \approx 1$. Moreover, most of the derived relative source abundances are in agreement with those derived by earlier groups.

In Sect. 5, we have studied the ratio of two primary species. The p/He ratio is explored both as a function of rigidity and of kinetic energy per nucleon. In the first case, the shape of the ratio is mostly ruled by the spallative reactions, while in the second case it is the solar modulation that shapes the observed ratio. We show that accurate measurements for the p/He ratio could help in the determination of the low energy shape of diffusion coefficient and source spectrum, especially if analysed as a function of rigidity.

Our analysis reinforces the need of more accurate data on light primary nuclei not only in the low-energy regime but also in the TeV/n-PeV/n range, as well as accurate measurement of primary-to-primary ratio. It would then be possible to significantly constrain the low-energy shape of the diffusion coefficient and the source spectrum, and fix the asymptotic behaviour of propagated nuclei.

Acknowledgements. We thank Alexander Panov for providing us an ASCII file of the ATIC data and Makoto Hareyama for providing us the RUNJOB and other experiment data points. D. M. thanks Laurent Derome and William Gillard for useful comments and discussions on the paper.

References

- Ahn, H. S., Allison, P., Bagliesi, M. G., et al. 2009, *ApJ*, 707, 593
- Ahn, H. S., Allison, P., Bagliesi, M. G., et al. 2010a, *ApJ*, 714, L89
- Ahn, H. S., Allison, P. S., Bagliesi, M. G., et al. 2010b, *ApJ*, 715, 1400
- Ahn, H. S., Allison, P. S., Bagliesi, M. G., et al. 2008, *Astroparticle Physics*, 30, 133
- Alcaraz, J., Alpat, B., Ambrosi, G., et al. 2000, *Physics Letters B*, 490, 27
- AMS Collaboration, Aguilar, M., Alcaraz, J., et al. 2002, *Phys. Rep.*, 366, 331
- AMS Collaboration, Alcaraz, J., Alpat, B., et al. 2000, *Physics Letters B*, 494, 193
- Asakimori, K., Burnett, T. H., Cherry, M. L., et al. 1998, *ApJ*, 502, 278
- Ave, M., Boyle, P. J., Gahbauer, F., et al. 2008, *ApJ*, 678, 262
- Ave, M., Boyle, P. J., Höppner, C., Marshall, J., & Müller, D. 2009, *ApJ*, 697, 106
- Binns, W. R., Wiedenbeck, M. E., Arnould, M., et al. 2008, *New A Rev.*, 52, 427
- Binns, W. R., Wiedenbeck, M. E., Arnould, M., et al. 2005, *ApJ*, 634, 351
- Boezio, M., Bonvicini, V., Schiavon, P., et al. 2003, *Astroparticle Physics*, 19, 583
- Boezio, M., Carlson, P., Francke, T., et al. 1999, *ApJ*, 518, 457
- Caprioli, D., Amato, E., & Blasi, P. 2010, *Astroparticle Physics*, 33, 160
- Derbina, V. A., Galkin, V. I., Hareyama, M., et al. 2005, *ApJ*, 628, L41
- Diehl, E., Ellithorpe, D., Müller, D., & Swordy, S. P. 2003, *Astroparticle Physics*, 18, 487
- Donato, F., Maurin, D., Brun, P., Delahaye, T., & Salati, P. 2009, *Physical Review Letters*, 102, 071301
- Donato, F., Maurin, D., Salati, P., et al. 2001, *ApJ*, 563, 172
- Donato, F., Maurin, D., & Taillet, R. 2002, *Astronomy and Astrophys.*, 381, 539
- Drury, L. O. 1983, *Reports on Progress in Physics*, 46, 973
- Duvernois, M. A. & Thayer, M. R. 1996, *ApJ*, 465, 982
- Dwyer, R. & Meyer, P. 1987, *ApJ*, 322, 981
- Ellison, D. C., Drury, L. O., & Meyer, J.-P. 1997, *ApJ*, 487, 197
- Engelmann, J. J., Ferrando, P., Soutoul, A., Goret, P., & Juliusson, E. 1990, *A&A*, 233, 96
- Ferrand, G., Downes, T., & Marcowith, A. 2008, *MNRAS*, 383, 41
- George, J. S., Lave, K. A., Wiedenbeck, M. E., et al. 2009, *ApJ*, 698, 1666
- Gilmore, G., Gustafsson, B., Edvardsson, B., & Nissen, P. E. 1992, *Nature*, 357, 379
- Gupta, M. & Webber, W. R. 1989, *ApJ*, 340, 1124
- Haino, S., Sanuki, T., Abe, K., et al. 2004, *Physics Letters B*, 594, 35
- Herbst, K., Kopp, A., Heber, B., et al. 2010, *Journal of Geophysical Research (Space Physics)*, 115
- Ichimura, M., Kogawa, M., Kuramata, S., et al. 1993, *Phys. Rev. D*, 48, 1949
- Ivanenko, I. P., Shestoporov, V. Y., & et al. 1993, *ICRC*, 2, 17
- Jones, F. C. 1994, *ApJS*, 90, 561
- Jones, F. C., Lukasiak, A., Ptuskin, V., & Webber, W. 2001, *ApJ*, 547, 264
- Lemoine, M., Vangioni-Flam, E., & Casse, M. 1998, *ApJ*, 499, 735
- Lionetto, A. M., Morselli, A., & Zdravkovic, V. 2005, *Journal of Cosmology and Astro-Particle Physics*, 9, 10
- Maurin, D., Donato, F., Taillet, R., & Salati, P. 2001, *ApJ*, 555, 585
- Maurin, D., Putze, A., & Derome, L. 2010, *A&A*, 516, A67
- Maurin, D., Taillet, R., & Donato, F. 2002, *Astronomy and Astrophys.*, 394, 1039
- Menn, W., Hof, M., Reimer, O., et al. 2000, *ApJ*, 533, 281
- Meyer, J.-P., Drury, L. O., & Ellison, D. C. 1997, *ApJ*, 487, 182
- Mueller, D., Swordy, S. P., Meyer, P., L'Heureux, J., & Grunsfeld, J. M. 1991, *ApJ*, 374, 356
- Nath, B. B. & Biermann, P. L. 1994, *MNRAS*, 267, 447
- Ogliore, R. C., Stone, E. C., Leske, R. A., et al. 2009, *ApJ*, 695, 666
- Osborne, J. L. & Ptuskin, V. S. 1988, *Soviet Astronomy Letters*, 14, 132
- Padovani, M., Galli, D., & Glassgold, A. E. 2009, *A&A*, 501, 619
- Panov, A. D., Adams Jr., J. H., Ahn, A. S., et al. 2009, *Bulletin of the Russian Academy of Sciences: Physics*, 73, 564
- Perko, J. S. 1987, *A&A*, 184, 119
- Ptuskin, V. S., Moskalenko, I. V., Jones, F. C., Strong, A. W., & Zirakashvili, V. N. 2006, *ApJ*, 642, 902
- Putze, A., Derome, L., & Maurin, D. 2010, *A&A*, 516, A66
- Putze, A., Derome, L., Maurin, D., Perotto, L., & Taillet, R. 2009, *A&A*, 497, 991
- Sanuki, T., Motoki, M., Matsumoto, H., et al. 2000, *ApJ*, 545, 1135
- Scherer, K., Fichtner, H., Ferreira, S. E. S., Büsching, I., & Potgieter, M. S. 2008, *ApJ*, 680, L105
- Seo, E. S. & Ptuskin, V. S. 1994, *ApJ*, 431, 705
- Shikaze, Y., Haino, S., Abe, K., et al. 2007, *Astroparticle Physics*, 28, 154
- Swordy, S. P., Mueller, D., Meyer, P., L'Heureux, J., & Grunsfeld, J. M. 1990, *ApJ*, 349, 625
- Wang, J. Z., Seo, E. S., Anraku, K., et al. 2002, *ApJ*, 564, 244
- Webber, W. R. 1987, *A&A*, 179, 277
- Webber, W. R. 1998, *ApJ*, 506, 329
- Webber, W. R., Cummings, A. C., McDonald, F. B., et al. 2008, *Journal of Geophysical Research (Space Physics)*, 113, 10108
- Webber, W. R., Golden, R. L., & Stephens, S. A. 1987, *ICRC*, 1, 325
- Webber, W. R. & Higbie, P. R. 2009, *Journal of Geophysical Research (Space Physics)*, 114, 2103
- Webber, W. R. & Lezniak, J. A. 1974, *Ap&SS*, 30, 361
- Webber, W. R., Lukasiak, A., & McDonald, F. B. 1997, *ApJ*, 476, 766
- Webber, W. R., Soutoul, A., Kish, J. C., & Rockstroh, J. M. 2003, *ApJS*, 144, 153
- Zatsepin, V. I., Adams, J. H., Ahn, H. S., et al. 2003, *ICRC*, 4, 1829
- Zatsepin, V. I., Zamchalova, E. A., & et al. 1993, *ICRC*, 2, 13